

1
2 **Simulating aerosol lifecycle impacts on the subtropical**
3 **stratocumulus-to-cumulus transition using large eddy simulations**
4

5 **Ehsan Erfani¹, Peter Blossey¹, Robert Wood¹, Johannes Mohrmann¹, Sarah J. Doherty^{1,2},**
6 **Matthew Wyant¹, Kuan-Ting O¹**

7
8 ¹Department of Atmospheric Sciences, University of Washington, Seattle, WA, USA

9 ²Cooperative Institute for Climate, Ocean and Ecosystem Studies, University of Washington,
10 Seattle, WA, USA

11
12 Correspondence to: Ehsan Erfani, (Erfani@uw.edu)

13
14 **Key points:**

15 • An LES is used to study the response of clouds to initial and boundary aerosol perturbations in
16 two marine stratocumulus to cumulus transition cases.

17 • Although the interactive aerosol scheme within the LES adds new degrees of freedom, the results
18 agree well with observations.

19 • Precipitation regulates the sensitivity to aerosols and the relative contributions of cloud
20 adjustments to radiative forcing.

1 **Abstract**

2 A Large Eddy Simulation (LES) model that simulates the aerosol lifecycle, including aerosol
3 sources and sinks, was used to study the stratocumulus to cumulus transition (SCT). To initialize,
4 force, and evaluate the LES, we used a combination of reanalysis, satellite, and aircraft data from
5 the Cloud System Evolution in the Trades field campaign in summer 2015 over the Northeast
6 Pacific. The simulations follow two Lagrangian trajectories from initially overcast stratocumulus
7 to the tropical shallow cumulus region near Hawaii.

8 The first trajectory is characterized by an initially clean, well-mixed stratocumulus-topped marine
9 boundary layer (MBL), then continuous MBL deepening and precipitation onset followed by a
10 clear SCT and a consistent reduction of aerosols that ultimately leads to an ultra-clean layer in the
11 upper MBL. The second trajectory is characterized by an initially polluted and decoupled MBL,
12 weak precipitation, and a late SCT. Overall, the LES simulates the general MBL features seen in
13 observations. Sensitivity studies with different aerosol initial and boundary conditions reveal
14 aerosol-induced changes in the transition, and albedo changes are decomposed into the Twomey
15 effect and adjustments of cloud liquid water path and cloud fraction. Impacts on precipitation play
16 a key role in the sensitivity to aerosols: for the first case, runs with enhanced aerosols exhibit
17 distinct changes in microphysics and macrophysics such as enhanced cloud droplet number
18 concentration, reduced precipitation, and delayed SCT. Cloud adjustments are dominant in this
19 case. For the second case, enhancing aerosols does not affect cloud macrophysical properties
20 significantly, and the Twomey effect dominates.

21

1 **1 Introduction**

2 Low marine clouds are the most widespread clouds on Earth, and they significantly affect the
3 Earth's radiation balance by strongly reflecting sunlight (Wood, 2012). They are also the main
4 source of uncertainty in cloud feedback across global climate models (Bony and Dufresne, 2005;
5 IPCC, 2013; Zelinka et al., 2017), largely due to the necessary use of physics parameterizations
6 that represent subgrid processes in those models. Stratocumulus (Sc) clouds are the predominant
7 type of low marine cloud over the eastern subtropical oceans where the shallow and often well-
8 mixed marine boundary layer (MBL) lies between cold surface ocean water and a strong capping
9 inversion induced by the strong subsidence of warm and dry air aloft (Bretherton et al. 2004;
10 Wood, 2012).

11 As Sc clouds are transported westward and equatorward by Trade winds, the warmer ocean water
12 enhances surface latent heat fluxes, making the MBL deeper and decoupled, with shallow cumulus
13 (Cu) clouds rising into an Sc layer below the inversion. Enhanced buoyancy within the Sc layer,
14 penetrative entrainment by Cu updrafts, and weakened subsidence above the inversion cause
15 stronger entrainment of dry air from the free troposphere (FT) and the eventual dissipation of the
16 Sc cloud (Krueger et al., 1995; Bretherton and Wyant, 1997; Wyant et al., 1997; Zhou et al. 2015).
17 This phenomenon, called the Sc-to-Cu transition (SCT), has been investigated by numerous studies
18 over the previous decades to understand the underlying microphysical and macrophysical
19 processes and the sensitivity of the transition to effects such as downward longwave radiative
20 fluxes, inversion strength (Sandu and Stevens, 2011) and large-scale subsidence (van der Dussen
21 et al., 2016). It is very challenging for weather and climate models to accurately simulate SCTs
22 because of the complex set of physical mechanisms and feedbacks driving the transition (Hannay
23 et al., 2009; Texeira et al., 2011; Lin et al., 2014; Kubar et al., 2015). Large Eddy Simulation (LES)

1 is a useful tool for studying SCTs due to its ability to resolve turbulence and cloud processes in
2 the MBL (Sandu and Stevens, 2011; Berner et al., 2013; Blossey et al., 2013; Yamaguchi and
3 Feingold, 2015; Yamaguchi et al., 2017, hereafter Y17; Blossey et al., 2021, hereafter B21).

4 Aerosols can significantly alter Sc clouds and SCTs. As explained by the first aerosol indirect
5 effect or Twomey effect (Twomey 1977; Platnick and Twomey, 1994), anthropogenic aerosols
6 cause an increase in cloud droplet number concentration (N_c) and a decrease in cloud droplet size,
7 which enhances cloud albedo when macrophysical cloud properties (e.g. liquid water path (LWP)
8 and cloud fraction (CF)) are unchanged. Albrecht (1989) concluded that the resulting smaller cloud
9 droplets would suppress precipitation since they have lower collision-coalescence efficiency.
10 However, the changes (known as adjustments) in LWP, CF, precipitation, and entrainment
11 generate complex aerosol-cloud interactions beyond simply precipitation suppression (Stevens and
12 Feingold, 2009; Gryspeerdt, et al., 2019; Wood, 2021), and this full set of adjustments can partly
13 or fully offset the Twomey effect on albedo (e.g., Glassmeier et al., 2021). These adjustments in
14 LWP and CF to changes in aerosol can therefore lead to either positive or negative cloud radiative
15 forcing depending on the ambient meteorological and aerosol conditions (Ackerman et al., 2004;
16 Wood, 2007; Wood, 2021).

17 Previous studies concluded that precipitation can be an important factor in the occurrence of SCT
18 (Xue et al., 2008; Wood et al., 2011; Yamaguchi and Feingold, 2015). Using an LES, Y17
19 highlighted the impact of precipitation on aerosols since collision-coalescence removes not just
20 cloud droplets but also aerosols, leading to further enhancement of drizzle in the aerosol-depleted
21 clouds. Using aircraft observations, Wood et al., (2018) confirmed this and showed that such
22 removal of aerosols results in the development of ultra-clean layers (UCLs), thin and horizontally
23 extensive layers below the MBL inversion during SCT with unactivated aerosol number

1 concentration less than 10 cm^{-3} in the absence of clouds or N_c less than 10 cm^{-3} in the presence of
2 clouds.

3 The desire to understand the factors controlling Sc cloud properties and SCTs has motivated
4 intensive observational field campaigns and LES studies along Lagrangian trajectories. The first
5 Lagrangian measurements of SCTs were conducted using aircraft-based observations during the
6 Atlantic Stratocumulus Transition Experiment (ASTEX) over the northeast Atlantic Ocean in June
7 1992 (Albrecht et al., 1995). Those observations showed that drizzle and dry air above the
8 inversion are important in Sc breakup during SCTs (Bretherton et al., 1999). A recent field
9 campaign, the Cloud System Evolution in the Trades (CSET), was conducted over the Northeast
10 Pacific in the summer of 2015 (Albrecht et al., 2019; Bretherton et al., 2019). To track the evolution
11 of air masses during CSET, flights used a track-and-resample strategy: a westward flight by the
12 National Science Foundation (NSF)/National Center for Atmospheric Research (NCAR)
13 Gulfstream GV aircraft sampled the MBL and lower FT offshore of California using in-situ and
14 remote sensing instruments to measure microphysical and macrophysical characteristics of
15 aerosols and clouds. Then, the Hybrid Single-Particle Lagrangian Integrated Trajectory
16 (HYSPLIT) model was used to construct multiple quasi-Lagrangian forward trajectories (the
17 trajectories are quasi-Lagrangian because they are based on the wind at the 500 m height to
18 represent MBL air movement; for simplicity, hereafter we call them Lagrangian trajectories). The
19 return flight was then planned to intersect and re-sample the same MBL air parcel two days later
20 near Hawaii.

21 Mohrmann et al. (2019; hereafter M2019) studied 53 Lagrangian trajectories during CSET using
22 satellite and reanalysis products in addition to the aircraft data. That analysis indicated that the
23 CSET cases were representative of the region's summer-time cloud fraction and inversion strength.

1 They also highlighted two Lagrangian cases for modeling studies: L06, a clean case with an
2 initially well-mixed MBL and a clear SCT; and L10, a polluted case with an initially decoupled
3 MBL and much slower cloud evolution. B21 selected these two cases and conducted LES
4 experiments along Lagrangian trajectories using prescribed N_c . The reason for prescribing N_c was
5 the high spatial and temporal variability in aerosol concentration during CSET (Bretherton et al.
6 2019) and the absence of aerosol boundary conditions outside of the two aircraft flights. On the
7 other hand, Y17 demonstrated that an LES with a fixed N_c leads to a slow SCT because, by design,
8 it does not include the drizzle enhancement due to the aerosol removal via the collision-
9 coalescence process.

10 In this study, we build on B21 and conduct Lagrangian LES experiments that include a treatment
11 of the aerosol lifecycle to explore the aerosol-cloud-precipitation interactions for two well-
12 observed case studies, and we evaluate how these case studies respond to perturbed aerosol initial
13 and boundary conditions. Our LES experiments benefit from a prognostic aerosol model (Berner
14 et al., 2013) that simulates aerosol budget tendencies of a single aerosol mode and predicts N_c . The
15 present research is part of the Marine Cloud Brightening (MCB) project, which studies the
16 potential feasibility and efficacy of climate intervention via the deliberate injections of sea-salt
17 spray into the MBL to hinder global warming by enhancing N_c and consequently cloud albedo. It
18 was shown previously that a 5% absolute increase in low cloud cover would be adequate to
19 counteract the global warming caused by CO₂ doubling (Slingo 1990; Wood 2012). However, the
20 enhancement of aerosols may also affect LWP and cloud fraction depending on the aerosol
21 distribution and ambient meteorological conditions, which could affect the climate impact of such
22 aerosol enhancements. This study aims to evaluate the model through comparisons with in situ and
23 remote sensing observations and to shed light on the mechanisms of cloud albedo response to

1 perturbed aerosols under two distinct sets of ambient meteorological conditions. In Section 2, a
2 description of the observational data and LES experimental design is presented. The simulation
3 results are explained in Section 3. These results are then interpreted to explore SCT by precipitation
4 in Section 4 and the decomposition of aerosol-cloud effects in Section 5. Finally, conclusions are
5 given in Section 6.

6

7 **2 Data and Methods**

8 **2.1 Data**

9 The LES experiments in this study are based on the CSET field campaign, which took place in
10 July and August 2015 over the Northeast Pacific (Albrecht et al., 2019). The simulations follow
11 Lagrangian HYSPLIT trajectories from the subtropical Sc deck region offshore of California to
12 the tropical shallow Cu region near Hawaii (Figure 1). Specifically, they follow the two trajectories
13 constructed by M2019 noted above: L06-Tr2.3¹ (hereafter L06 for simplicity), as a clean case, and
14 L10-Tr6.0 (hereafter L10) as a polluted case. These trajectories have been extended to include
15 periods before and after the intersection of the research flights with trajectories L06 and L10.
16 Trajectory L06 was sampled by research flight RF06 and then, two days later, by research flight
17 RF07, while L10 was sampled in a similar manner by RF10 and RF11. In-situ aircraft
18 measurements presented in this study are from a flight leg that descended from the lower FT into
19 the sub-cloud layer during the intersection of the flight with the Lagrangian trajectory. This
20 represents a short sampling time (half an hour or less) but provides valuable information about

¹ For each CSET case, multiple trajectories are provided, but in this study we select only one trajectory for each case. Therefore, we denote each trajectory by their case name.

1 microphysics and macrophysics of aerosol-cloud interactions. The data from this flight path is
2 presented as a single vertical profile for each intersection with the HYSPLIT trajectory.

3 Observational and reanalysis data are used for both forcing and verifying the Lagrangian LES.
4 Meteorological and thermodynamic variables are extracted from the European Center for Medium-
5 Range Weather Forecasts (ECMWF) ERA5 reanalysis data (Hersbach et al., 2020). Cloud LWP,
6 CF, and surface and top of atmosphere (TOA) radiative fluxes were obtained from the
7 Geostationary Operational Environmental Satellite (GOES; Minnis et al., 2008) retrievals, with a
8 horizontal resolution of 5 km and temporal resolution of 5 minutes², and from Clouds and the
9 Earth's Radiant Energy System (CERES) – Synoptic TOA and surface fluxes and clouds (SYN) –
10 level 3 product (Doelling et al. 2016) with a horizontal resolution of 1° and temporal resolution of
11 1 hour. The Special Sensor Microwave Imagers (SSMI; Wentz et al., 2012) with a maximum
12 occurrence of 8 times per day and band-dependent horizontal resolution (from 15×13 to 69×43
13 km), and the Advanced Microwave Scanning Radiometer (AMSR; Kawanishi et al., 2003) with a
14 maximum occurrence of 2 times per day and band-dependent horizontal resolution (from 5×3 to
15 62×35 km), were used as additional sources of observed LWP. In addition, we use precipitation,
16 derived from AMSR 89 GHz brightness temperature for shallow marine clouds, which is available
17 twice daily with a horizontal resolution of 10 km (Eastman et al., 2019), and we use cloud-top
18 height (CTH) retrieved from MODIS, available twice daily with the horizontal resolution of 1°
19 (Eastman et al., 2017). The Modern-Era Retrospective analysis for Research and Applications,
20 Version 2 (MERRA2; Gelaro et al., 2017) reanalysis provides aerosol properties with a horizontal
21 resolution of 0.5°×0.625° and a temporal resolution of 3 hours, as generated from the Goddard

² GOES data are available at this temporal resolution, but we interpolate them to the time-step of the trajectories, which is hourly.

1 Chemistry Aerosol Radiation and Transport (GOCART) model, which assimilates meteorological
2 data and satellite observations. We calculate the accumulation-mode N_a using the MERRA-2
3 aerosol per-species mass and the MERRA-2 assumed particle size distribution. The resulting
4 MERRA2 N_a are then calibrated through regression against N_a measurements from all the CSET
5 flight data (See Appendix A). To compile satellite and reanalysis datasets along the trajectories,
6 each variable is averaged over a $2^\circ \times 2^\circ$ box that is centered over the trajectory at each time. The
7 spread in the SSMI and AMSR variables is presented as a standard deviation within that box,
8 whereas the spread in GOES variables is calculated as the range in the averages across five $2^\circ \times 2^\circ$
9 boxes centered on and around the trajectory at each time.

10 Here, we define a few terms and variables that will be discussed later. First, SCT is defined as the
11 first time low cloud cover (LCC) drops below 50% and remains below 50% for 24 hours after that
12 or until the end of the simulation (whichever is shorter). This definition excludes purely diurnal
13 LCC fluctuations. Second, the inversion height (Z_{inv}) is calculated as the height where $(\frac{d\theta_l}{dz})(\frac{dRH}{dz})$
14 is minimized. θ_l is liquid-water potential temperature and RH is relative humidity (B21). Finally,
15 the entrainment rate (w_e) is calculated as: $w_e = (dZ_{inv}/dt) - w_{ls,inv}$ where dZ_{inv}/dt is the
16 tendency of Z_{inv} , and $w_{ls,inv}$ is the large-scale vertical velocity at Z_{inv} (B21).

17

18 **2.1 Model**

19 We use the System for Atmospheric Modeling (SAM; Khairoutdinov and Randall, 2003) version
20 6.10.9 to conduct the LES experiments. Our simulations with SAM use the Morrison et al. (2005)
21 microphysics without ice phase hydrometeors or processes, the Rapid Radiative Transfer Model
22 for Global Climate Models (RRTMG; Mlawer et al. 1997), and cloud optical parameterizations

1 from the Community Atmosphere Model version 5 (CAM5; Neale et al. 2010). Berner et al. (2013)
2 coupled the Morrison microphysics to a single-mode bulk (log-normal) aerosol scheme that
3 predicts the mass and number mixing ratios of the accumulation mode aerosol in three categories:
4 unactivated, within-cloud-droplet, and within-rain-drop, by calculating tendencies due to
5 activation, coalescence scavenging (accretion), autoconversion, interstitial scavenging, surface
6 sources, and sedimentation. The present simulations include two changes from Berner et al (2013).
7 First, the combined number and mass mixing ratios of unactivated and within-cloud-droplet
8 aerosol (N_a and q_a , respectively) are chosen as prognostic variables rather than the number and
9 mass mixing ratios of unactivated aerosol. The number mixing ratio of unactivated aerosol is
10 computed as the difference between N_a and N_c , and the mass mixing ratio of unactivated aerosol
11 is diagnosed from the combined lognormal size distribution of unactivated and within-cloud-
12 droplet aerosol assuming that the unactivated aerosol occupies the small tail of the size distribution.
13 Second, while the surface flux of aerosol number is unchanged from Berner et al (2013), the
14 surface flux of aerosol mass is corrected to have a characteristic geometric mean dry diameter of
15 220 nm.

16 The simulations are performed along L06 and L10, starting at ~ 0.75 days before the westward
17 flight intersection (start time is 17 July 2015, 01Z for L06 and 27 July 2015, 00Z for L10), and
18 they are run until ~ 1 day after the return flight intersection, for a total simulation time of ~ 3.75
19 days. The number of vertical levels is 432, with the highest resolution (10 m) from 950 m to
20 3800 m to better capture the complex processes during the evolution of the MBL top. The
21 horizontal resolution is 100 m for all the simulations. Two horizontal domain sizes are used:
22 $9.6 \times 9.6 \text{ km}^2$ for a total of 12 runs, and $25.6 \times 25.6 \text{ km}^2$ (denoted LD for larger domain) for a total
23 of 4 runs (Table 1). The LES simulations are forced with sea surface temperature (SST) (Fig. 1),

1 geostrophic winds, large-scale vertical velocity (W), and large-scale horizontal advection of
2 temperature and moisture from the ERA5 reanalysis (Fig. 1 in B21). Note that the trajectory is
3 computed based on the velocity at a single height, so wind shear can lead the large-scale advective
4 tendencies to be non-zero away from that height. Initial profiles of temperature and moisture are
5 based on aircraft data in the MBL and ERA5 data aloft, with a blending between the two in the
6 lower free troposphere. See B21 for details. From the initialization time until the time of the
7 westward flight intersection, the LES temperature and total water mixing ratio profiles are nudged
8 to the aircraft profiles on a 3-hour time scale to allow the LES to develop a cloud-topped well-
9 mixed MBL by the time of the westward flight arrival, but after that time, the temperature,
10 moisture, and aerosol within the MBL evolve freely, without any nudging. Throughout the
11 simulation, the temperature, moisture, and aerosol profiles in the free troposphere are also nudged
12 towards a combination of observations and reanalysis starting 500 m above the inversion. A weak
13 nudging of the winds is applied: throughout the simulation, the domain-averaged winds are nudged
14 to ERA5 profiles on a 12-hour time scale. See B21 for more details on the LES configurations.

15 For each trajectory, one LES simulation is conducted with aerosols prescribed based on in situ
16 observations at the time of the first research flights, so that the LES would simulate realistic initial
17 N_c . In the simulation labeled L06 40-40, the FT and initial MBL N_a are identical at 40 mg^{-1} , while
18 L10 250-60 has initial MBL $N_a=250 \text{ mg}^{-1}$ and FT set to $N_a=60 \text{ mg}^{-1}$ throughout the simulation.
19 Note that each run is labeled by its initial MBL N_a and FT N_a in that order. In other runs, N_a is
20 varied to test the sensitivity of the LES simulations to perturbations in the MBL and FT aerosols.
21 See Table 1 for a full list of simulations. While the FT N_a in the LES is relaxed to these prescribed
22 values throughout the simulation starting 500 m above the inversion, the aerosols within the MBL
23 are allowed to evolve freely so that rapid changes in N_a and N_c , as seen in Y17, can be captured.

1 In addition to simulations with these prescribed two-layer aerosol profiles based on in-situ
2 observations, we also conduct simulations using time-varying vertical profiles of N_a from
3 MERRA2 to initialize the MBL N_a and force the FT N_a in order to develop a framework for running
4 LES purely based on reanalysis products in the absence of any aircraft observations. These
5 profiles, which are computed using the method in Appendix A, are shown in Figure 2 along with
6 in situ observations of N_a from the research flights. Although MERRA2 captures the general
7 features of the aircraft N_a measurements, significant biases exist at certain times and heights.
8 Further comparison of MERRA2 and in-situ N_a is provided in Appendix A (Figure A1).
9 Nonetheless, the MERRA2 aerosols can provide a useful constraint on N_a in remote locations when
10 no aircraft measurements are available.

11

12 **3 Results**

13 For each L06 or L10 case, a run is selected as the reference and its evolution and comparison with
14 observations are described in more detail. Then, various runs are compared and the sensitivity to
15 aerosol concentration and domain size is explained. A reference run for each case is selected from
16 the larger-domain runs, using the run that simulates MBL N_a and N_c closest to that from the aircraft
17 and GOES observations at the time of westward aircraft. Based on this criterion, the reference run
18 is 40-40-LD for case L06 (as seen in Figures 3a&b and Figures 4a&b) and the 250-60-LD for case
19 L10 (Section 3.2). By studying the reference run for each case, we investigate if the reference run
20 is able to simulate a realistic evolution of N_a and N_c and whether it can estimate the meteorological
21 features similar to observations.

22

1 3.1 L06 Case

2 3.1.1 Reference Run (40-40-LD)

3 This run is initialized with clean MBL and FT conditions and simulates a consistent reduction of
4 MBL-averaged³ aerosol and cloud droplet number concentrations (e.g. $\langle N_a \rangle$ and $\langle N_c \rangle$) (Figs.
5 3a&b). This ultimately leads to the formation of a UCL at the top of MBL at the time of the return
6 flight intersection (Figs. 4a&b), in agreement with aircraft aerosol observations and also the
7 observational analysis of Wood et al. (2018). This is a successful test of SAM when using the
8 prognostic bulk aerosol model (B21 used prescribed values of N_c in its simulations, and therefore
9 the ability of SAM to simulate UCL could not be tested). The UCL formation is explored in more
10 detail in Section 4.

11 The trend of decreasing simulated $\langle N_a \rangle$ along the trajectory is similar to that seen in the aircraft-
12 based observations. Although $\langle N_a \rangle$ from the MERRA2 reanalysis decreases with time,
13 concentrations are twice the in-situ $\langle N_a \rangle$ at the time of the initial flight and three times larger than
14 the in-situ measured $\langle N_a \rangle$ at the time of the return flight. The reduction in simulated $\langle N_c \rangle$ along
15 the trajectory seems to occur slightly faster than in the observations. Similar to the aircraft
16 observations, the GOES retrieved N_c decreases along the trajectory, but the retrieved values are
17 somewhat lower than the aircraft-derived $\langle N_c \rangle$, possibly due to biases from cloud inhomogeneities
18 over the $9 \times 9 \text{ km}^2$ retrieval footprint due to broken clouds (Bretherton et al., 2019).

19 Figures 3d-f illustrate the time series of MBL-averaged aerosol budget tendencies⁴ of N_a . Here,
20 scavenging is the summation of accretion, autoconversion, and interstitial scavenging. For the

³ The MBL-average of each variable is calculated as a density-weighted average of that variable from surface to inversion height (Z_{inv}): $\langle A(t) \rangle = \frac{\int_0^{Z_{inv}} A(z,t) \rho(z,t) dz}{\int_0^{Z_{inv}} \rho(z,t) dz}$, where z is height, t is time, and ρ is air density.

⁴ In this study, budget tendencies include the total effect of un-activated aerosols, cloud droplets and rain drops.

1 reference run, accretion is the strongest among these three terms, and autoconversion and
2 interstitial scavenging have comparable values⁵. The sedimentation term is not shown, because its
3 column-averaged values are negligible. For the reference run, the entrainment term is small,
4 because the aerosol gradient between the MBL and FT is negligible initially. By the time this
5 gradient increases the clouds have mostly dissipated and therefore entrainment remains weak after
6 the second night. Scavenging is a stronger sink, causing decreases in $\langle N_a \rangle$ and $\langle N_c \rangle$ that contribute
7 to precipitation onset right before the second night (Fig. 5b). The surface is a strong source of
8 aerosol in the first 12 hours of all runs because the surface winds are strong (figure not shown).
9 This counteracts the accretion sink and leads to a slight increase in $\langle N_a \rangle$ and $\langle N_c \rangle$ over the first
10 night.

11 The L06 40-40-LD reference run simulates the general observed trend towards the SCT as
12 quantified by comparing the domain-averaged LCC from the simulations and as retrieved from
13 GOES (Fig. 5a). However, it has an overall underestimation in LCC from GOES on the first
14 simulated day. In addition, the simulated SCT onset is early by about half a day, leading to an LCC
15 underestimation up to the time of return flight observations (day 2.75), suggesting that the positive
16 precipitation feedback in the prognostic aerosol scheme might be too strong. This is also reflected
17 in the comparison of the SW CRE (defined as all-sky minus clear-sky net SW at TOA) (Fig. 3c):
18 although the simulated SW CRE from the reference run decreases from day one to day three, the
19 simulated CRE is biased low relative to the CERES retrieval on day two, due to earlier cloud
20 breakup⁶ in the simulation. The simulated accumulated surface precipitation (Fig. 5b) for L06 40-
21 40-LD is 0.5-2 mm less than the AMSR precipitation throughout the simulation but is within the

⁵ This is generally true for all the runs.

⁶ In this study, cloud breakup refers to the reduction of domain-averaged LCC from 80% to 20%.

1 AMSR uncertainty (1 standard deviation). The reference run shows precipitation onset a few hours
2 before the SCT (on the second night) (Fig. 5a) when the cloud droplet effective radius (r_e) exceeds
3 15 μm (figure not shown). This value is sometimes used as a threshold radius for the production
4 of significant precipitation in marine low clouds (see Masunaga et al., 2002, and references
5 therein). Precipitation continued until the end of the run but is stronger during the night. This is
6 consistent with the clear diurnal cycle of LWP (Fig. 5d), w_e (Fig. 5e), and turbulence (w'^2) (figure
7 not shown): all three are stronger during the night. As will be discussed later, these changes in
8 precipitation are closely related to changes in entrainment and cloud LWP (Blossey et al., 2013
9 and references therein)

10 The three LWP observational products (GOES, SSMI, and AMSR) agree well most of the time
11 (Fig. 5d). Although the simulated LWP in the L06 40-40-LD run is generally lower than the
12 observed values (the exceptions are from day 0.5 to day 0.75 and the last few hours of simulations
13 when SSMI and the LES values agree well), it is mostly within the uncertainty range of the
14 SSMI/AMSR values. A general decrease in LWP is apparent during the SCT in both the reference
15 run and the observed products.

16 The evolution of the simulated Z_{inv} (Fig. 5c) is very similar to that in ERA5 in the first 24 hours of
17 the simulations because of the nudging that occurs until day 0.75. However, due to the early SCT,
18 subsequent MBL deepening in the reference run is slightly slower than in ERA5, leading to an
19 ultimate underestimation Z_{inv} of 700 m relative to ERA5. As a result, the modeled w_e is generally
20 lower than the ERA5 w_e . Although the reference run is biased low relative to the domain-averaged
21 values of GOES and MODIS CTH most of the time, it has better agreement with the 75th percentile
22 GOES CTH, which represents Cu towers after the SCT.

1 Despite these biases, the outgoing longwave radiation (OLR) in the L06 40-40-LD run agrees well
2 with CERES observations most of the time (Fig. 5f). The TOA albedo also agrees well with the
3 CERES-derived albedo (not shown) on the first day, but underestimates the observation after that,
4 due to early SCT and LCC underestimation in this run.

5 The vertical profiles of observed and modeled relative humidity (RH) are illustrated in Figs. 4c&d
6 at the times of westward and return flights, respectively. The LES runs were nudged toward the
7 aircraft profiles from the start until day 0.75. Still, the LES develops a sharper inversion (e.g.
8 vertical gradient of variables near the inversion is stronger) and slightly moister MBL profiles at
9 the time of the westward flight.

10 Two days after the nudging ends, the reference run (L06 40-40-LD) successfully simulates the
11 moisture profile in the MBL as observed from the aircraft, with the exception of the MBL top,
12 where LES Z_{inv} is ~ 500 m shallower than aircraft Z_{inv} . This is due to the early SCT that slows
13 down the MBL deepening. The ERA5 profile within the MBL is drier and slightly warmer,
14 compared to aircraft profiles.

15 Maps of cloud LWP across the model domain demonstrate the evolution of scattered Cu clouds
16 from Sc clouds along the L06 trajectory (Fig. S1). Before the SCT and near the westward flight
17 time, closed cells are dominant across the domain. A day later (after the SCT), a few bigger cells
18 with cores of strong LWP and precipitation exist along with small patches of Cu clouds scattered
19 throughout the domain. This pattern does not change much until the simulation finish time and is
20 also seen at the time of the return flight.

21 The evolution of MBL height and thermodynamics, and the structure of mesoscale organizations
22 in our reference run are very similar to the LES result of Lx29 from B21 that used the same settings

1 as our reference run (with the exception of using a prescribed N_c and slightly larger domain size,
2 i.e., 29 km) (their Figs. 7-8). However, our reference run shows an earlier and faster SCT (Figs.
3 S2b&c), because the prognostic aerosol scheme in our LES represents the positive precipitation
4 feedback that leads to a faster decrease in N_c than is given by the linear reduction rate of N_c from
5 40 to 10 mg^{-1} , prescribed in B21-Lx29 (Fig. S2). The prognostic N_c plays a key role in the SCT:
6 Y17 conducted idealized LES sensitivity experiments based on a composite Lagrangian trajectory
7 over the Northeast Pacific with prognostic and fixed N_c (their Fig. 10) and showed that the SCT
8 does not occur in runs with fixed N_c because the precipitation feedback does not exist in those
9 runs. Overall, the LES experiments of Y17 that include prognostic N_c show the evolution of the
10 SCT in agreement with our results (e.g. a reduction of N_c , a 12-hour cloud breakup, and
11 precipitation onset; see their Fig. 3). However, their LES displays a sudden decrease in N_c during
12 the SCT and complete shut-down of MBL deepening afterward, neither of which are seen here.
13 The latter might be due to the constant-in-time subsidence in Y17, in contrast to time-varying
14 subsidence with a net ascent at low levels (<1500 m) between westward and return flights in this
15 study.

16

17 **3.1.2. Effects of Perturbed Aerosol Initial and Boundary Conditions**

18 Several sensitivity simulations have been made with different initial and boundary conditions for
19 aerosol, and these runs are described in Table 1. The runs with enhanced N_a (e.g. MERRA,
20 MERRA-LD, and MERRAx3) exhibit distinct changes in microphysics and macrophysics. An
21 increase in initial N_a among the different runs leads to enhanced N_c and therefore smaller r_e (figure
22 not shown), which then results in a suppression of the aerosol scavenging term (Fig. 3e).
23 Consequently, enhanced N_a and N_c are associated with stronger entrainment, deeper MBLs,

1 increased turbulence, delayed precipitation onset and reduced accumulated precipitation, and
2 ultimately a delayed SCT (Fig. 5). This is consistent with the LES study of Goren et al. (2019)
3 and the observational study of Christensen et al. (2020) which also found that aerosols prolong
4 cloud lifetime and increase cloud albedo, causing a delay in SCT. The Lagrangian LES runs by
5 Y17 and B21 also are consistent with our study in terms of the sensitivity to N_c . Also, Sandu and
6 Stevens (2011) did an LES sensitivity study wherein they decreased N_c from 100 to 33 cm^{-3} and
7 found that the increased precipitation in the latter run hastens the SCT considerably (their Fig. 8).
8 This agrees with the delay in the SCT with increased N_a and N_c and suppressed precipitation seen
9 here. Although MERRA-LD simulates the timing of SCT more accurately compared to the
10 reference run, this is achieved at the expense of biased aerosols both at the initial time and during
11 the run.

12 Using an LES, Sandu et al. (2008) concluded that increased aerosols also produce stronger
13 turbulence and therefore a more well-mixed MBL, which causes stronger entrainment and MBL
14 deepening. Moreover, perturbing N_c seems to modify entrainment through precipitation: by
15 removing liquid water from the entrainment zone, precipitation acts to restrict entrainment, making
16 it difficult to cool and moisten FT air and incorporate it into the MBL. Therefore, runs with
17 enhanced N_c and suppressed precipitation also have larger Z_{inv} (Albrecht, 1993; Stevens and
18 Seifert, 2008; Blossey et al, 2013).

19 With a strong N_a gradient between the MBL and FT, the entrainment term in the N_a budget
20 becomes important, as seen in the MERRAx3 run with high MBL N_a (Fig. 3d). A pollution layer
21 (possibly smoke) was transported above the inversion in the MERRA2 reanalysis dataset on day
22 2 (Fig. 2a), but this is too late in the LES simulation to significantly impact the simulated MBL
23 aerosol concentrations. This is because, despite a strong N_a gradient at the inversion level at the

1 time of return flight for the MERRA and MERRA-LD runs (Fig. 4b), the entrainment becomes
2 negligible after the inversion cloud breakup and precipitation onset (Fig. 3d).

3 The initial FT N_a has an important role in controlling the MBL N_c , as a large FT N_a increases the
4 MBL N_c through the enhanced entrainment of FT aerosols into the MBL when still in the Sc cloud
5 regime. This addition of aerosols from the FT can be sufficient to counter the loss of MBL aerosol
6 by scavenging processes, as simulated by the 40-150 run (time-series not shown, but mean values
7 are presented in Fig. 9). However, increasing FT N_a later in the simulation, as in the 40-40to150
8 run, has little impact in this case, and the clouds evolve very similarly to those in the 40-40 run.

9 Unlike in the reference run, LES runs with a larger initial N_a simulate precipitation onset despite
10 having r_e much smaller than $15\ \mu\text{m}$ (figure not shown). This was previously explained by Wood
11 et al. (2009) (their Fig. A3): with high values of N_c and LWP, there is no need for r_e to exceed the
12 value of $15\ \mu\text{m}$ for precipitation onset.

13 At the time of the westward flight, the RH profiles of various LES runs are all almost identical
14 (Fig. 4c) because of nudging to aircraft profiles. However, at the time of return flight (Fig. 4d),
15 runs with enhanced N_a have larger Z_{inv} , reflecting the influence of precipitation on inversion height
16 (Albrecht, 1993). The increased entrainment in these runs is also associated with stronger MBL
17 decoupling and a drier MBL.

18

19 **3.1.3. Effects of Domain Size**

20 Here, we compare two larger-domain runs (40-40-LD and MERRA-LD) with their smaller-domain
21 counterparts (40-40 and MERRA). Looking at 40-40-LD and 40-40, the effect of domain size is

1 modest for a number of metrics: number concentrations time series ($\langle N_a \rangle$ and $\langle N_c \rangle$; Figs. 3a-b),
2 RH profiles (Fig. 4), precipitation onset (Fig. 5c), and SCT initiation onset (Fig. 5a). However, 40-
3 40-LD does exhibit a stronger accretion sink (Fig. 3e) and stronger precipitation on the second
4 night. Furthermore, MBL deepening (Fig. 5c) is slower in 40-40-LD on the second night, and
5 therefore, w_e is smaller (Fig. 5e). Two days into the run, when the SCT has occurred (LCC \sim 20%),
6 the two runs become almost identical until the end of the simulation.

7 The effect of domain size is more pronounced in runs initialized and forced with higher aerosol
8 concentrations (MERRA-LD and MERRA runs). $\langle N_a \rangle$ and $\langle N_c \rangle$ in these runs are more than twice
9 that measured from the aircraft at the time of westward flight, but the rate of aerosol reduction in
10 MERRA-LD is faster so that $\langle N_a \rangle$ and $\langle N_c \rangle$ in the MERRA-LD run are half of that in the smaller-
11 domain MERRA run, and very close to that from the observations, at the time of return flight (Fig.
12 3a&b). The vertical profiles of $\langle N_a \rangle$ and $\langle N_c \rangle$ reveal that the MERRA-LD run has UCLs at the
13 time of the return flight (Fig. 4a&b). This change in aerosol tendencies seems to be related to
14 precipitation: stronger accretion in MERRA-LD over the first two days leads to earlier
15 precipitation onset and cloud breakup (by about 12 hours) when compared to the MERRA run. At
16 the end of the simulation, accumulated precipitation in MERRA-LD is 25% larger than that in the
17 MERRA run (Fig. 5b). An earlier SCT in the MERRA-LD run leads to lower albedo and smaller
18 w_e , resulting in shallower Z_{inv} . The earlier occurrence of an SCT in simulations with larger domains
19 was also reported in previous studies (e.g. Y17; B21).

20 Differences in the evolution of cloud morphology in the smaller and larger-domain MERRA runs
21 play a role in the different SCT timing (Fig. S3). Mesoscale organization quickly emerges in the
22 MERRA-LD run (Fig. S3m). The MERRA run cannot simulate the mesoscale structure due to its
23 small domain size. This is also reflected in the Probability distribution functions (PDFs) of cloud

1 LWP and N_c (Figs. S3a&h) from the two runs, which are broader for MERRA-LD, with higher
2 probability of larger LWP and smaller N_c in MERRA-LD compared with the MERRA run. Overall,
3 a positive feedback is implied: the early broadening at the upper end of the LWP PDF in MERRA-
4 LD run (Figs. S3a&b) is associated with precipitation initiation in larger LWP bins on days 0.5
5 and 1, and this drives the scavenging of aerosols (Figs. S3e&f). The resulting clean MBL facilitates
6 further precipitation formation, leading to onset of the SCT, when the broadening intensifies for
7 both the LWP and $\langle N_c \rangle$ PDFs, along with the significant increase in precipitation on day 2 of the
8 run (Figs. S3c&g&o). The broadening of PDFs in the MERRA run is negligible until day 2 which
9 is a few hours before SCT.

10

11 **3.2 L10 Case**

12 **3.2.1 Reference Run (250-60-LD)**

13 This case is characterized by an initially polluted MBL. Based on Figs. 6a&b, we selected 250-60-
14 LD as the reference run, because it is the larger-domain run that simulates MBL N_a and N_c closest
15 to the observations. The reference run simulates the overall trend of decreasing $\langle N_a \rangle$ and $\langle N_c \rangle$
16 over the Lagrangian trajectory, though the rate of reduction in $\langle N_c \rangle$ is slower than in the
17 observations. The modeled $\langle N_c \rangle$ agrees quite well with GOES $\langle N_c \rangle$ on the first day, and the
18 difference with GOES $\langle N_c \rangle$ does not exceed 50% on the second and third days. Uncertainties in
19 instantaneous satellite estimates of N_c are likely to exceed 80% (Grosvenor et al., 2018), which is
20 the approximate difference between the observed N_c values from the aircraft and satellite. As such,
21 the observed and LES N_c values agree to within measurement uncertainty.

1 The rate of reduction in $\langle N_a \rangle$ and $\langle N_c \rangle$ is insufficient to form a UCL in the reference run, nor is a
2 UCL seen in the aircraft data (Figs. 7a&b). This is in contrast with the L06 case, where an initially
3 cleaner MBL leads to a UCL (Figs. 4a&b). Looking at N_a , the reference run lies within the range
4 of observations in the subcloud layer at the time of both flights (Fig. 7a&b) but underestimates the
5 aircraft observations within the cloud layer at the time of westward flight (day 0.67). At the time
6 of return flight, it under-estimates the aircraft N_a in the lower part of the cloud layer but
7 overestimates N_a and N_c just below the inversion.

8 The time series of MBL-averaged aerosol budget tendencies of N_a (Figs. 6d-f) for the reference
9 run demonstrates that the scavenging term (with the largest contribution from accretion) is a strong
10 sink in the first and last 18 hours of the simulation, and its enhancement later in the simulation
11 corresponds to non-negligible precipitation (Fig. 8b). Initially, the entrainment term is a strong
12 aerosol sink in the reference run due to the aerosol gradient between the MBL and FT, but as the
13 MBL N_a decreases with time, so does the MBL-FT gradient; therefore, the entrainment term
14 becomes negligible towards the end of the run. Similar to the L06 case, the surface flux of aerosol
15 in L10 is maximized at the beginning of the simulation, but it is more than five times weaker than
16 the L06 case due to weaker surface winds.

17 The vertical profile of modeled RH (Fig. 7c) is similar to the aircraft profile at the time of westward
18 flight due to the nudging of the simulation but is slightly moister than aircraft below the Sc cloud
19 layer. At the time of return flight (Fig. 7d), the modeled MBL is slightly drier and deeper than seen
20 by the aircraft.

21 At the time of the return flight, RH values observed from the aircraft are high (50-90%) above the
22 inversion (Fig. 7d), consistent with the advection of moisture from an adjacent convective system.

1 However, this moist layer is absent in the ERA5 profiles at this time, with RH values much lower
2 (less than 50%) above the inversion for ERA5 and the reference run (which is nudged to ERA5
3 starting 500m above the inversion). such a layer is delayed in ERA5.

4 The evolution of Z_{inv} (Fig. 8c) shows that the reference run under-predicts the inversion height
5 relative to that from ERA5 in the first 24 hours of the simulations, then a deeper MBL after this.
6 The modeled MBL deepens gradually after day 2.3, but the ERA5 MBL shows negligible
7 deepening until day 3.2, and then it suddenly grows over a few hours, due to the moisture advection
8 from an adjacent convective system. The result is that the modeled and ERA5 Z_{inv} are close at the
9 end of the simulation. The reference run overestimates the mean values of GOES CTH from the
10 westward flight time until about 18 hours later, and underestimates that from day 2.0 until the end
11 of simulation. Kubar et al. (2020) showed that observed CTH and Z_{inv} from satellite retrievals are
12 very similar in the Sc region, but Z_{inv} is higher than CTH in the Cu region because some Cu clouds
13 do not reach the inversion level.

14 The 250-60-LD reference run presents a strong diurnal cycle as seen by cloud breakup, reduced
15 LWP, and enhanced OLR during the daytime, and vice versa during the nighttime for the first 60
16 hours of simulation (Figs. 8a&d&f). Observations exhibit a weaker diurnal cycle: GOES shows
17 overcast conditions on the first day and a delayed cloud breakup on the second day (Fig. 8a). As a
18 result of this discrepancy, the reference run overestimates the daytime CERES OLR and
19 underestimates the daytime SW CRE (Fig. 6c) in that time range. Both model and GOES LCC
20 exhibit overcast condition on the third day, and therefore modeled and CERES OLR and SW CRE
21 agree relatively well. On the last night, the reference run has a stronger cloud breakup than GOES.

1 This coincides with precipitation onset (Fig. 8b), followed by reduction in LWP (Fig. 8d) and
2 entrainment rate (Fig. 8f) showing the occurrence of SCT in this run ⁷.

3 The horizontal distribution of LWP (Fig. S1) demonstrates an overcast Sc layer during the spin-
4 up (day 0.6), followed by the emergence of closed cells as seen on days 1.6 and 2.6. On day 3.6
5 and after the SCT, the Sc layer has dissipated and a combination of a few bigger cells and smaller
6 patches of Cu exists within the domain. The reference run generally under-predicts LWP relative
7 to GOES, with the two agreeing only for a few hours before the SCT late in the daytime on
8 simulation day 3. Since the GOES LWP observations are only available for daytime, it isn't
9 possible to test for model bias in LWP relative to GOES during the following nighttime. The
10 modeled LWP is also generally smaller than SSMI and AMSR LWP during the daytime and larger
11 than those during the nighttime (with the exception of the second night), but agrees well with those
12 products in some instances of early morning and early night (e.g. around days 0.7, 2.5, 3.0 and,
13 following the SCT, on day 3.6). The AMSR accumulated precipitation (Fig. 8b) shows that weak
14 precipitation exists at all times over the trajectory, but stronger precipitation is seen in the first and
15 last 12 hours. The 250-60-LD is only able to capture the observed signal in the last 12 hours.
16 Ultimately, the reference run underestimates the AMSR precipitation by 2 mm, but it is within the
17 observed uncertainty (1 standard deviation).

18 In order to understand the effect of interactive aerosols vs. prescribed N_c , we compare our reference
19 run, 250-60-LD, with the Lx29 run from B21 for the L10 case. Overall, there is good agreement
20 between our reference simulation and the B21-Lx29 for thermodynamic profiles, MBL growth,

⁷ For the reference run, we do not have 24 hours of simulation after the cloud breakup to show that LCC remains below 50%. However, the late cloud breakup occurs during the night and right after precipitation onset and this is different than day-time cloud breakups that has no precipitation. Therefore, we can say with good confidence that the last instance of cloud breakup for the reference run is SCT.

1 and the mesoscale organization (figures not shown). Although both studies were initialized with
2 similar aerosols, the rate of N_c reduction in our reference run is faster than that in B21 in the first
3 24 hours (Fig. S2d) because an accretion sink (Fig. 6e) and weak precipitation (Fig. 8b) during this
4 time lead to aerosol removal in our reference run.

5 The two runs have a very similar cloud structure (Figs. S2e&f) until 12 hours before the simulation
6 ends, when the B21-Lx29 simulation demonstrates thinning of Sc clouds, and our reference run
7 shows Sc cloud breakup. Precipitation onset in B21-Lx29 occurs about 12 hours earlier than that
8 in our reference run (figure not shown), however the use of prescribed N_c in B21-Lx29 (a constant
9 value of 60 mg^{-1} in the last 24 hours of simulation) causes a slow reduction of CF. In contrast, the
10 coupled aerosol scheme in our reference run simulates a significant reduction of N_c (e.g. a domain
11 average of about 30 mg^{-1} in the last 24 hrs of the run, and a lower bound marked by standard
12 deviation reaching to 1 mg^{-1}) prompting cloud breakup. This highlights the advantage of using a
13 prognostic aerosol scheme in LES.

14

15 **3.2.2. Effects of N_a and N_c**

16 As in L06, the L10 case was simulated with differing aerosol initialization and boundary conditions
17 to understand its sensitivity to aerosol perturbations. Although enhancing N_a in the simulations of
18 L10 (e.g., MERRA, MERRAx3) leads to distinct changes in microphysics [e.g., an increase in N_c
19 (Fig. 6b) and consequent enhancement of cloud optical depth and reduction of r_e (figures not
20 shown)] and radiation [e.g., enhanced SW CRE (Fig. 6c)], it does not affect meteorological
21 variables significantly. It is only in the last 12 hours of the 3.75-day simulations that the runs show
22 a slight enhancement of Z_{inv} and entrainment rate and reduction of precipitation and OLR with
23 increasing N_a (Fig. 8). Such weak sensitivity of cloud macrophysical properties to N_a in this case

1 is in contrast with the L06 case, and seems to be related to the lack of precipitation-driven diabatic
2 changes due to the higher N_a in the L10 reference case. However, reducing the initial MBL N_a
3 from 250 mg^{-1} to 70 mg^{-1} , as in the 70-60 run, leads to an early reduction in N_c (Fig. 6b) and
4 induces the formation of the UCLs at the time of westward flight (Fig. 7a), consistent with sudden
5 enhancement of scavenging sink (Fig. 6e), precipitation onset and SCT occurrence during the spin-
6 up of this run (Fig. 8). For the rest of simulation, the LWP remains too low to permit the Sc layer
7 restoration, and therefore larger OLR and smaller entrainment rate and Z_{inv} values are seen in this
8 run.

9

10 **3.2.3. Effects of Domain Size**

11 As in the L06 case, to test for sensitivity to model domain size we developed two pairs of
12 simulations, with each pair was run with identical forcings, but different domain sizes (e.g. 250-
13 60-LD and 250-60 as the first pair, and 70-60-LD and 70-60 as the second pair). Comparing 250-
14 60-LD and 250-60, the latter does not simulate an SCT (similar to the large and small domain
15 simulations of this case in B21). In fact, the reduction of $\langle N_a \rangle$ and $\langle N_c \rangle$ with time (Figs. 6a&b) is
16 slightly faster in 250-60-LD due to a stronger (albeit still relatively modest) accretion sink (Fig.
17 6e) and precipitation (Fig. 8b) in the first and last 12 hours of this run. Near the end of this run, the
18 precipitation is strong enough to reduce LWP and cause an SCT, and as a result, 250-60-LD has
19 shallower MBL, larger OLR, and weaker entrainment rate in the last 12 hours. Although
20 precipitation in the L10 case is much weaker than that in the L06 case, the 250-60-LD run
21 accumulates ~ 3 times more precipitation than the 250-60 run.

22 Both the 70-60-LD and 70-60 runs simulate an SCT very early on, but the former shows slightly
23 earlier cloud breakup and precipitation onset (Fig. 8) associated with faster reduction of $\langle N_a \rangle$ and

1 $\langle N_c \rangle$ and stronger accretion sink (Fig. 6) in the first 12 hours. After the first day, the two runs are
2 very similar until the end. Ultimately, the 70-60-LD run produces about 25% more accumulated
3 precipitation than the 70-60 run, mainly during the SCT, highlighting the ability of larger domains
4 to support a broader distribution of LWP and precipitation.

5 Consistent with the L06 case and previous studies (e.g. Y17 and B21), larger-domain runs in the
6 L10 case simulate an earlier occurrence of SCT than the small-domain runs, and this is associated
7 with greater mesoscale organization in the larger-domain runs, as seen in the cloud morphology
8 (Figs. S4m-p) in 250-60-LD after day 2.5. Similar to the L06 MERRA-LD run, a positive feedback
9 exists between cloud LWP, precipitation, and $\langle N_c \rangle$: A broader PDF of LWP leads to stronger
10 precipitation, i.e. more values in larger LWP bins, that consequently remove aerosols and
11 encourage further precipitation, until the SCT in 250-60-LD, when LWP and $\langle N_c \rangle$ PDFs become
12 much broader and precipitation occurs in all LWP bins.

13

14 **3.3 Sensitivity of cloud fields to aerosols**

15 Sections 3.1 and 3.2 cover the LES fidelity in representing the cloud fields, which is a primary
16 goal of this study. In this Section, we look at the sensitivity of the results to the aerosol, which is
17 the secondary goal of this study. The domain-averaged time-mean of various variables as a
18 function of $\langle N_c \rangle$ for all the LES simulations in this study is depicted in Figure 9. Negligible
19 macrophysical sensitivity to $\langle N_c \rangle$ is seen for runs with the mean $\langle N_c \rangle$ larger than $\sim 150 \text{ mg}^{-1}$, as
20 is the case in most of the L10 simulations. Larger $\langle N_c \rangle$ inhibits precipitation and slows the removal
21 of aerosols by autoconversion and accretion, and therefore its further increase has a minimal effect
22 on cloud macrophysical features. This differs from the findings of Xue et al. (2008), who simulated

1 an idealized version of an Atlantic Trade Wind Experiment (ATEX) case that exhibited a decrease
2 in LCC with N_c for N_c greater than 100 mg^{-1} . The LCC decrease in Xue et al. (2008) is not related
3 to precipitation. Instead, the shorter evaporative timescale for small drops is invoked as an
4 explanation: clouds with higher N_c and smaller r_c more readily evaporate. Our LES uses a
5 saturation adjustment approach, and so cannot represent this effect. It does, however, represent the
6 effects of droplet sedimentation (Bretherton et al., 2007) which could, in principle, yield a similar
7 result. More recent LES studies seem to call into question the importance of drop size-dependent
8 evaporation on entrainment rate and cloud macrophysical responses (Williams and Igel, 2021),
9 suggesting that thermal infrared radiative impacts of different drop sizes may be responsible. Such
10 effects are captured in our LES simulations. Thus, it is currently unclear whether we might obtain
11 N_c -induced decreases in LCC in our LES under some meteorological conditions.

12 Increasing $\langle N_c \rangle$ leads to an enhancement of the short-wave cloud radiative effect (SW CRE; which
13 is equal to all-sky minus clear-sky net SW at TOA) in both trajectories, but as $\langle N_c \rangle$ increases the
14 rate of change in the CRE decreases (Fig. 9a). This is due in part to weaker albedo susceptibility
15 for high $\langle N_c \rangle$ (Twomey and Platnick, 1994; see Sec. 3.5), but the weakening cloud adjustments
16 for $\langle N_c \rangle$ greater than $\sim 100 \text{ mg}^{-1}$ (Figs. 9b&c) are also a major reason.

17 The decrease in mean precipitation with increasing $\langle N_c \rangle$ in our LES runs (Fig. 9d) is very similar
18 to that given in Fig. 1 in Wood (2005). That study presented a collection of various in situ aircraft
19 and remote sensing observations from different locations around the world, and found that polluted
20 cases (N_c greater than 100 mg^{-1}) correspond to precipitation less than 0.1 mm day^{-1} , whereas clean
21 cases ($N_c \sim 20 \text{ mg}^{-1}$) are associated with precipitation $\sim 1 \text{ mm/day}$.

1 The responses of LWP to increasing $\langle N_c \rangle$ in L06 and L10 have opposite signs for large $\langle N_c \rangle$:
2 LWP increases with $\langle N_c \rangle$ for L06 but decreases with $\langle N_c \rangle$ in L10 for $\langle N_c \rangle$ greater than 100 mg^{-1}
3 (Fig. 9b). This is qualitatively consistent with the behavior seen for precipitating and non-
4 precipitating regimes identified in previous works (e.g. Toll et al. 2017; Hoffmann et al. 2020),
5 though here we find a weaker decrease in LWP with $\langle N_c \rangle$. Overall, LWP increases with $\langle N_c \rangle$
6 when $\langle N_c \rangle$ is less than 100 mg^{-1} . For larger $\langle N_c \rangle$, LWP shows a weak decrease with $\langle N_c \rangle$ but
7 remains near 70 g m^{-2} .

8 An increase in mean LCC with an increase in mean $\langle N_c \rangle$ for precipitating runs highlights the
9 positive precipitation feedback, explained in Sections 3.1 and 3.2. Looking at the LCC and
10 precipitation time series for L06, their onset is delayed with the increase in $\langle N_c \rangle$, so that time-
11 mean LCC increases with $\langle N_c \rangle$ (Figs. 5a&b). This is not the case for L10, because there is no SCT
12 and precipitation (except for a few runs, including the reference run), and the LCC does not vary
13 much with $\langle N_c \rangle$.

14 These results are broadly consistent with the LES results of Ackerman et al. (2003), and Ackerman
15 et al. (2004). Although they simulated cases from different field campaigns with different domain
16 sizes and resolutions, they showed that suppressed N_c corresponds to enhanced precipitation, and
17 reduced turbulence and entrainment. Ackerman et al. (2003) showed a strong dependence of LCC,
18 LWP, and precipitation on N_c when N_c falls below 50 cm^{-3} . Similarly, all variables shown in Fig.
19 9 have stronger sensitivity to N_c for smaller N_c . In addition, the regulation of Z_{inv} by precipitation,
20 as outlined by Albrecht (1993), is evident: the runs with stronger precipitation have shallower
21 MBLs, and the runs with no precipitation have similar Z_{inv} .

22

1 4 SCT by precipitation

2 Feingold and Kreidenweis (2002) noted the efficient removal of aerosol by precipitation for clean
3 cases and called it the “runaway precipitation” process. LES simulations of the transition from
4 closed to open cells by Berner et al. (2013) exhibited similar behavior, followed by suppressed
5 turbulence and entrainment in the resulting low-aerosol MBL. Furthermore, Y17 expressed the
6 importance of precipitation onset in initializing SCT via the “SCT by precipitation” hypothesis.
7 Here, we investigate this in more detail by examining the SCT during two of our LES runs.

8 Figure 10 presents time-height plots of w'^2 , N_a , CF, and precipitation flux contours before and after
9 SCT⁸ for two runs (L06 MERRA-LD and L10 250-60-LD). The non-precipitating Sc cloud layer
10 before the SCT has a thickness of 300-500 m and shows enhanced turbulence (as quantified by
11 w'^2 , which is strongest in the upper half of MBL). The turbulence reaches its peak right before the
12 SCT, associated with convection and formation of Cu clouds (Wood, 2012). This is followed by
13 precipitation onset and a coincident decrease in MBL CF and cloud-layer N_a . This implies that the
14 precipitation-induced reduction in aerosols enhances the breakup of the inversion cloud. The L06
15 MERRA-LD run produces a UCL, but the near-inversion N_a in the L10 250-60-LD remains larger
16 than 10 mg^{-1} after the SCT. Nevertheless, this is consistent with Fig. 2 in Ackerman et al. (2003),
17 which shows that overcast Sc clouds are unsustainable when N_c falls below about 50 mg^{-1} .

18 Compared to the L06 MERRA-LD run, the inversion cloud breakup in the L10 250-60-LD run is
19 faster and stronger: near-inversion CF values for L06 MERRA-LD remain between 40 and 50% a
20 few hours after the SCT, whereas they drop below 20% for L10 250-60-LD. This seems to be

⁸ As a reminder, we define SCT as the first time LCC drops below 50% and remains below 50% for 24 hours after that or until the end of simulation (whichever is shorter).

1 related to the deeper MBL in the latter case. As stated by Eastman and Wood (2016), CF in a
2 shallow precipitating MBL is more persistent than in deep precipitating MBLs. Figures 10g-h
3 depict the vertical profiles of the probability distribution functions of N_a at a few times near the
4 SCT. It is seen that the N_a distribution begins broadening near the inversion about 0.8 days before
5 the SCT. By the time of the SCT, the layer with a broader N_a distribution extends to lower levels,
6 showing that the ultra-clean layers that first appear near the inversion spread through much of the
7 cloud layer.

8 For each of the two runs shown in Fig. 10, a time near the SCT with significant surface
9 precipitation is selected and maps of surface precipitation and cloud LWP for the LES domain are
10 displayed in Figs. 11a&b and 12a&b. LWP has local maxima in the cores of mesoscale cells, where
11 strong precipitation occurs. A transect is selected for each map and vertical cross-sections of N_a
12 (non-activated plus within-cloud-droplet aerosol), N_c , rain water mass (q_r), and cloud water mass
13 (q_c) are shown in Figs. 11c&d and 12c&d. In both runs, the remaining Sc clouds (thickness ~ 500
14 m) and shallow Cu clouds (depth ~ 1500 m) coexist, and precipitation is prevalent in both. The Cu
15 cells contain relatively large N_a and N_c , but UCLs (N_a and $N_c < 10 \text{ mg}^{-1}$) develop near the Cu towers
16 and overall, the near-inversion N_a and N_c remain low ($< 30 \text{ mg}^{-1}$) throughout the transect. These
17 results are in agreement with O et al. (2018), who used an idealized parcel model and showed that
18 the formation of UCLs in the inversion layer is caused by collision-coalescence in the updraft
19 parts of trade Cu, and this diminishes N_c .

20 Figure S5 shows time-series of cloud cover, cloud LWP, and precipitation for all of the runs from
21 both L06 and L10 that exhibit a clear SCT. Here, time 0 shows the point identified as the SCT for
22 each run. In the two hours before SCT, the LCC and LWP start decreasing rapidly at the same time
23 as the onset of precipitation. During the SCT, the domain-averaged LWP is between 40 and 60 g

1 m^{-2} , and surface precipitation in the Cu cores (quantified as the 95th percentile precipitation)
2 exceeds 20 mm day^{-1} for most runs. Observational studies have shown that marine Sc precipitation
3 at cloud base increases with LWP and decreases with N_c (see Wood, 2012 and references therein).
4 Comstock et al. (2004) and Wood et al. (2011) showed that $\text{LWP} \langle N_c \rangle^{-1}$ is a good indicator of
5 precipitation from satellite data. Our LES runs suggest that $\text{LWP} \langle N_c \rangle^{-1}$ exceeding $\sim 10 \text{ g m}^{-2} \text{ cm}^3$
6 in the Cu cores can be a predictor of SCT (Fig. S5c). Looking at Fig. 10 in Comstock et al. (2004)
7 and using their power-law relation between $\text{LWP} N_c^{-1}$ and precipitation based on radar
8 observations, $\text{LWP} N_c^{-1}$ of $10 \text{ g m}^{-2} \text{ cm}^3$ yields precipitation equal to 21.5 mm day^{-1} , which is in
9 rough agreement with the 95th percentile precipitation rate in our LES results (Fig. S5d). Although
10 this value of precipitation is very high for marine low clouds, such values are quite common in
11 pockets of open cells, as shown by in-situ measurements of rain rates in the active and quiescent
12 cells (Fig. 22 in Wood et al., 2011). The results presented here show that the SCT is associated
13 with a reduction of N_a and N_c by precipitation and therefore suggest that aerosol is a key factor in
14 the LES simulations of SCT, and that a transition driven by precipitation is plausible.

15

16 **5 Decomposing Aerosol-cloud Effects**

17 To gain insights into the relative role of different mechanisms in cloud radiative forcing through
18 aerosols, we separate the cloud radiative effect into that caused by changes in N_c , LWP adjustment,
19 and CF adjustment respectively. We use the N_c effect as our best available approximation of the
20 Twomey effect because it is not possible to accurately calculate the Twomey effect in model
21 experiments with LWP and CF adjustments, since the Twomey effect is defined for fixed LWP
22 and CF.

1 To calculate each contribution, we assume two states: LES run 1 as the base state, and LES run 2
2 as the perturbed state. For the first step, we select the base state to be the reference run and the
3 perturbed state to be a run with modified (preferably, enhanced) aerosols. The change in cloud
4 albedo (α_c) due to N_c effect was calculated based on Eq. (2) in Wood (2021): $\Delta\alpha_c =$
5 $\frac{\alpha_{c_1}(1-\alpha_{c_1})(r_N^{1/3}-1)}{1+\alpha_{c_1}(r_N^{1/3}-1)}$, where r_N is the ratio of perturbed state cloud droplet number concentration
6 (N_{c_2}) to base state cloud droplet number concentration (N_{c_1}) (e.g. $r_N = \frac{N_{c_2}}{N_{c_1}}$). α_c can be related to
7 TOA cloudy-sky albedo (A_c) via Eq. (4) in Diamond et al. (2020): $A_c \approx \alpha_{ft} + \alpha_c \frac{t_{ft}^2}{1-\alpha_{ft}\alpha_c}$, where
8 α_{ft} is the albedo of the free troposphere (here, it is assumed to be a constant value of 0.05) and t_{ft}
9 is the transmissivity of the free troposphere and is calculated as $t_{ft} = \frac{F_{Z_{inv}}^\downarrow}{F_{TOA}^\downarrow}$, where $F_{Z_{inv}}^\downarrow$ is
10 downward SW flux at Z_{inv} and F_{TOA}^\downarrow is solar insolation. Thereafter, the cloud radiative forcing
11 (ΔR) due to the N_c effect can be calculated based on Eq. (17) in Diamond et al. (2020): $\Delta R_{N_c} =$
12 $-C_1 F_{TOA}^\downarrow \Delta A_c$, where C is cloud fraction.

13 A similar set of equations is used to calculate LWP adjustment, where in this case the $\Delta\alpha_c$ is
14 calculated as: $\Delta\alpha_c = \frac{\alpha_{c_1}(1-\alpha_{c_1})(r_L^{5/6}-1)}{1+\alpha_{c_1}(r_L^{1/3}-1)}$ where r_L is the ratio of perturbed state LWP (L_2) to base
15 state LWP (L_1) (e.g. $r_L = \frac{L_2}{L_1}$). Forcing for CF adjustment is calculated as: $\Delta R_{CF} = (C_2 -$
16 $C_1) F_{TOA}^\downarrow (A_{c_2} - A_{clear_2})$, where A_{clear} is clear-sky albedo. Finally, we calculate residual forcing
17 as: $\Delta R_{residual} = \Delta R_{N_c} + \Delta R_{LWP} + \Delta R_{CF} - \Delta R_{LES}$. A small residual is a good indicator of a
18 successful separation into the three components.

1 Forcing is non-linear with these properties, so its magnitude will depend on what is chosen as the
2 “base state”. Therefore, the forcing is calculated in a three-step process:

3 Step 1: ΔR is calculated with run 1 as the base state and run 2 as the perturbed state (as
4 explained above).

5 Step 2: ΔR is calculated with run 2 as the base state and run 1 as the perturbed state.

6 Step 3: ΔR is calculated as the average of the values from steps 1 and 2.

7 Figure 13 presents ΔA_c and ΔR calculated from the LES simulations as a function of r_N . Shown
8 are changes due to all cloud responses, and the contributions to the total from changes in N_c , LWP,
9 CF, as well as the residual between the sum of these and the total change. ΔA_c and ΔR increase
10 with r_N for both L06 and L10 cases, as does the contribution to ΔA_c and ΔR from the N_c changes,
11 meaning that the stronger the perturbed aerosol concentration, the stronger the cloud albedo and
12 cloud radiative forcing due to the N_c effect. This relationship is similar to the results of Wood
13 (2021; their Fig. 1) for the Twomey effect. Note that the ΔR - r_N relationship for the N_c effect is
14 dependent on both the ΔA_c - r_N relationship for N_c effect (square markers in Fig. 13) and the
15 average change in CF between the pair of runs (figure not shown, but can be inferred from Fig. 9).

16 The LWP adjustment enhances forcing with increasing r_N for L06, but the forcing is reduced with
17 increasing r_N for L10 (as is also evident in the LWP vs. $\langle N_c \rangle$ panel in Fig. 9). The CF
18 adjustment effect is very small for L10, but it is stronger than the N_c effect for L06, consistent with
19 the strong CF sensitivity to $\langle N_c \rangle$ for this case, as shown in Fig. 9. The different behaviors of
20 LWP and CF adjustments between the L06 and L10 cases seem to be related to precipitation:
21 strong precipitation in the L06 case regulates clouds through the removal of aerosols, and the
22 absence of precipitation in the L10 case means this feedback is also absent.

1 The CF values are very similar between the pairs of L10 LES runs, but the CF evolution differs
2 strongly for the pairs of L06 runs (hence the difference in the length of the error bars for forcing
3 through CF changes in Fig. 13). This also explains why the ΔR values associated with the N_c and
4 LWP effects differ significantly in the two calculations (step 1 versus step 2 above) for L06, but
5 not for L10.

6 Overall, it is seen that for the clean case (L06) all three effects contribute to the brightening, with
7 the CF adjustment being strongest and LWP adjustment weakest. This highlights the effect of
8 inhibiting the precipitation through enhanced N_c , which leads to increasing CF and LWP (Figs.
9 14a&c). In contrast, for the polluted case (L10), both ΔA_c and ΔR increase with N_c , and in the
10 absence of negligible CF adjustment (Fig. 14b), a negative LWP adjustment partially offsets the
11 Twomey effect (Fig. 14d). Ultimately, cloud brightening from the increase in N_c dominates for
12 L10. The negative LWP adjustment seems to be due to the continuation of MBL deepening and
13 decoupling in the absence of strong precipitation, which leads to evaporation of near-inversion
14 cloud liquid via entrainment (Ackerman et al., 2004; Xue et al., 2008).

15

16 **6 Conclusions**

17 Lagrangian LES experiments were developed and conducted along two subtropical MBL air mass
18 trajectories taken from the CSET field campaign (L06 and L10) in order to assess the ability of the
19 LES to reproduce the observed cloud evolution, and in particular to study the role of aerosol-cloud
20 interactions during the SCT. The LES results were evaluated against reanalysis, satellite, and in-
21 situ measurements. The LES used in this study includes a prognostic aerosol model that simulates
22 aerosol budget tendencies and provides a tool to test aerosol removal by precipitation (Wood et al.

1 2018) and SCT by precipitation (Y17). It also allows quantification of the roles of different
2 processes in two-way aerosol-cloud interactions.

3 For each of the two cases studied here, a “baseline” run was conducted that used initial aerosol
4 concentrations in the MBL and lower free troposphere that most closely matched those observed
5 from aircraft-based observations during CSET. The LES-simulated characteristics of cloud
6 evolution in the baseline L06 case are in general agreement with the observations. This is a clean
7 case, with both the model and observations showing a well-mixed Sc-topped MBL on the first day,
8 continuous MBL deepening, and precipitation onset after the first day followed by a clear SCT
9 and formation of UCLs. The simulated SCT occurs slightly earlier than in the observations, and
10 therefore the MBL is shallower. The LES simulates the cloud evolution in the L10 case with
11 somewhat less fidelity. This is a polluted case with a decoupled MBL and a strong diurnal cycle
12 in LCC. Based on LES, the MBL deepening intensifies after the second day and precipitation onset
13 and SCT occur only in the last 12 hours. Observations show slower MBL deepening and
14 continuous, but weak, precipitation throughout the simulation period.

15 Compared to previous studies with prescribed N_c (e.g. B21), the use of interactive aerosols in our
16 LES experiments adds new degrees of freedom, which makes it more challenging to reproduce the
17 observed trends. Nonetheless, these simulations are promising as they compare reasonably well
18 with observations. Capturing a strong two-way feedback between aerosols and precipitation in the
19 L06 case highlights the importance of including interactive aerosols. Furthermore, the use of
20 interactive aerosols in the model allows for diagnosing the relative roles of various processes in
21 driving aerosol concentration changes, providing guidance on useful metrics for comparisons to
22 other models and observations.

1 The sensitivity of the LES runs to aerosols is strongly dependent on whether there is precipitation
2 and on the aerosol concentration both within and above the MBL. For the clean, precipitating L06
3 baseline case, enhancement of MBL N_a (either through a larger initial MBL N_a or through the
4 entrainment of N_a from FT) leads to larger N_c , increased LWP, suppressed precipitation, and
5 delayed SCT. Aerosols impact on cloud variables is more significant for runs with smaller N_a
6 because precipitation change with aerosols is stronger for smaller N_a (Figure 9). However, for the
7 polluted, weakly-precipitating L10 baseline case⁹, increasing MBL N_a leads to distinct changes in
8 microphysics (e.g., enhancement of N_c and cloud optical depth, and reduction of r_e), but it causes
9 negligible effects on cloud macrophysical properties.

10 When the L10 case is run with lower initial aerosol concentrations, the model simulates
11 precipitation and a clear SCT early in the run. Larger-domain runs are conducted for both this case
12 and the precipitating L06 case. These runs are consistent with the hypothesis by Y17 that
13 precipitation is a driver of SCT, as the decrease in inversion-level clouds, N_a and N_c after the
14 precipitation onset implies that precipitation-induced reduction in aerosols enhances the breakup
15 of inversion cloud and the SCT.

16 Based on theoretical analyses from previous studies (e.g. Diamond et al., 2020; Wood, 2021), we
17 decomposed the contributions of the Twomey effect and cloud adjustments to albedo and SW
18 CRE. For both the L06 and L10 cases an increase in aerosols relative to the baseline case leads to
19 an increase in the SW CRE due to the Twomey effect. In contrast, both the sign and magnitude of
20 the SW CRE due to cloud adjustments depend strongly on the meteorological conditions (in

⁹ Indeed, this case is non-precipitating for the purpose of aerosol sensitivity test, because such test was conducted by enhancing N_a in small-domain runs and they simulated no significant precipitation. The runs with significantly low initial aerosols lead to precipitation.

1 particular, precipitation) of each case. For the L06 case, the SW CRE due to cloud adjustments
2 reinforces and is much larger than that of the Twomey effect, because the suppressed precipitation
3 delays the SCT. For the L10 case, the Twomey effect is dominant, with cloud adjustments only
4 moderately offsetting brightening from the increase in N_c . Here, the cloud adjustments are small
5 because the LCC does not change much with an increase in aerosols in this weakly-precipitating
6 polluted case, and the LWP decreases slightly.

7 The simulation of these two cases provides a framework for initializing and forcing LES using
8 meteorological and aerosol reanalysis data. Here, aircraft data were available as a second source
9 of aerosol and meteorological data. Comparisons of the aircraft and ERA reanalysis show
10 differences in the thermodynamic profile of the MBL. In addition, MERRA aerosols data is a
11 useful tool, but our simulations show the need for a tighter constraint on aerosols in remote regions.
12 While the L06 MERRA run performs reasonably well, it still simulates too high N_a early in the
13 run. The L10 MERRA run suggests an excessive FT N_a . Future work aims to simulate a larger
14 number of different Lagrangian trajectories under different meteorological and background aerosol
15 conditions to examine the extent to which the results presented here can be generalized.

16

17 **Acknowledgments**

18 This study was primarily supported by NOAA's Climate Program Office Earth's Radiation Budget
19 (ERB) Program, Grant ##NA20OAR4320271, as well as with funding from, Lowercarbon, the
20 Pritzker Innovation Fund, and SilverLining through the Marine Cloud Brightening Project. This
21 work used the Extreme Science and Engineering Discovery Environment (XSEDE), which is
22 supported by National Science Foundation grant number ACI-1548562, with some simulations

1 performed on Bridges2 at the Pittsburgh Supercomputing Center through allocation TG-
2 ATM190002. This publication is partially funded by the Cooperative Institute for Climate, Ocean,
3 & Ecosystem Studies (CIOCES) under NOAA Cooperative Agreement NA20OAR4320271,
4 Contribution No. 2022-1204. We appreciate Philip Rasch, Je-Yun Chun, Michael Diamond, and
5 Kyoungock Choi for discussions on this research that contributed to the improvement of the final
6 results.

7 CSET campaign data, including in-situ measurements, were provided by NCAR/EOL under the
8 sponsorship of the National Science Foundation and are available at
9 https://data.eol.ucar.edu/master_lists/generated/cset/. ERA5 data is available at
10 <https://cds.climate.copernicus.eu>. MERRA2 aerosol data can be obtained from
11 <https://disc.gsfc.nasa.gov/datasets>. AMSR and SSMI data are accessible at
12 www.remss.com/missions/. GOES data can be accessed from <https://www-angler.larc.nasa.gov/>.
13 CERES SYN1deg data were obtained from <https://ceres.larc.nasa.gov/>.

14

15 **Appendix A: Calculation of MERRA2 N_a**

16 **Part 1: Extracting N_a from the mass of different aerosol species**

17 MERRA2 aerosol data contains mass mixing ratio for 5 different species: dust, sea salt, organic
18 carbon (OC), black carbon (BC), and sulfate. For each OC and BC species, two different tracers
19 are available: hydrophilic and hydrophobic. Each dust and sea salt species is divided into 5 size
20 bins (Chin et al., 2002). Therefore, a total of 15 different aerosol tracers are provided in MERRA2
21 data (Table A1), and the total aerosol number concentration (N_a) is given by:

1

$$N_a = \sum_{t=1}^{15} N_t$$

2 where N_t is the number concentration for an individual aerosol tracer (in units of cm^{-3}) and is
 3 calculated as:

4

$$N_t = N_v \frac{\rho_a m_t}{\rho_t} \times 10^{12},$$

5 where ρ_a is air density (in units of kg m^{-3}), m_t is the mass mixing ratio of the tracer (in units of kg
 6 kg^{-1}), ρ_t is the density of tracer (in units of kg m^{-3}), and N_v is the number concentration divided by
 7 the total volume of that tracer:

8

$$N_v = \frac{N_0}{V_0},$$

9 where N_0 is the total number of particles per unit volume (in units of m^{-3}) and is calculated from
 10 Eq. (3) in Grainger (2012):

11

$$N_0 = \int_{r_d}^{r_u} n(r) dr,$$

12 where r is dry aerosol particle radius (in units of μm), $n(r)$ is the number density distribution (in
 13 units of $\text{m}^{-3} \mu\text{m}^{-1}$), r_d is lower radius, r_u is upper radius and V_0 is the total volume of particles per
 14 unit volume and is calculated from Eq. (19) in Grainger (2012):

15

$$V_0 = \int_{r_d}^{r_u} v(r) dr.$$

16 Here, $v(r)$ is the distribution of particle volume (in units of μm^{-1}) and is calculated as:

1
$$v(r) = \frac{4}{3}\pi r^3 n(r),$$

2 assuming spherical aerosol particles (Eq. 18 in Grainger, 2012). Note that each distribution in this
 3 study is a truncated distribution bounded by r_d and r_u for that tracer, and the integrations are
 4 solved following the composite trapezoidal rule.

5 For each OC, BC, and sulfate tracer, MERRA-2 assumes a lognormal distribution (Chin et al.,
 6 2002) which is calculated following Eq. (29) in Grainger (2012):

7
$$n(r) = \frac{N_0}{\sqrt{2\pi} \ln(\sigma_g) r} \exp\left\{-\frac{[\ln(r) - \ln(r_m)]^2}{2[\ln(\sigma_g)]^2}\right\},$$

8 where r_m is the modal radius and σ_g is the geometric standard deviation of the distribution.

9 For each dust tracer, with the exception of the smallest bin, a power distribution is assumed (per
 10 the MERRA2 FAQ webpage):

11
$$n(r) = \alpha r^\beta$$

12 where α and β are the power-law coefficient and exponent, respectively. Here, $\alpha = 1$ and $\beta =$
 13 -4 . For the smallest dust bin, a special treatment is considered as this bin is broken down into 4
 14 sub-bins. For each sub-bin, a similar power law is applied, but the mass for each sub-bin (m_s) is
 15 calculated as $m_s = w_m \times m_t$, where w_m is the mass weight for that sub-bin¹⁰.

¹⁰ w_m determines the contribution of each sub-bin to the total mass mixing ratio of the smallest dust bin. In other words, the summation of mass weights is equal to unity (Table A1).

1 For each sea-salt tracer, a modified gamma distribution is used (MERRA2 FAQ webpage) and
2 $n(r)$ is calculated following Eq. (2) in Gong et al. (2003):

$$3 \quad n(r) = r^{-A}(1 + 0.057r^{3.45}) \times 10^{1.607 \exp(-B^2)}$$

4 Where $A = 4.7(1 + \Theta r)^{-0.017r^{-1.44}}$ and $B = [0.433 - \log(r)]/0.433$ and Θ is a parameter that
5 controls the shape of sub-micron size distribution and is chosen to be equal to 30. All the required
6 parameters to calculate N_a (e.g. r_d , r_u , r_m , ρ_t , w_m , and σ_g) are provided in Table A1, and m_t and
7 ρ_a are extracted from MERRA2 aerosol data files. As a final note, our calculations are for r greater
8 than 50 nm.

9

10 **Part 2: Calibration of MERRA2 N_a using aircraft-based observations of N_a from CSET**

11 After calculating the MERRA2 total N_a from the mass of tracers in Part 1, we calibrate this N_a
12 using CSET aircraft-based observations of N_a . Data from all CSET flights are used for this
13 process. The accumulation mode aerosol number is calculated by selecting an aerosol diameter
14 greater than 80 nm. Observed N_a is calculated as the median value for each hour of aircraft data.
15 Then, the MERRA2 N_a is interpolated to the location of the flight data for each hour. The MBL
16 and FT data are separated by selecting the pressure (P) level of 700 hPa as a threshold for lower
17 FT and 850 hPa as a threshold for the top of MBL. For each MBL and FT section, MERRA2 N_a
18 is regressed against the aircraft-based N_a using a power-law fit (or linear fit in log-log space) (Fig.
19 A1). Higher skill is seen for the FT, with a correlation coefficient (R) of the fit equal to 0.67,
20 whereas R is equal to 0.56 in MBL. With the exception of low values of N_a (e.g. less than 3 cm^{-3}),
21 MERRA2 N_a underestimates aircraft N_a , and the underestimation increases with N_a . For example,

1 when the aircraft-based N_a is equal to 1000 cm^{-3} , N_a derived from MERRA2 is about 6 times
2 smaller than that in the MBL and about 3 times smaller than that in the FT. To correct for this bias,
3 the calibrated MERRA2 N_a is calculated as:

$$4 \quad N_{a_{\text{calib}}} = \begin{cases} \exp(1.43 \ln(N_a) - 0.25), & P \geq 700 \text{ hPa} \\ \exp(1.20 \ln(N_a) - 0.08), & P \leq 850 \text{ hPa} \end{cases}$$

5

6 **References**

- 7 Ackerman, A.S., Toon, O.B., Stevens, D.E. and Coakley Jr, J.A., 2003: Enhancement of cloud cover and
8 suppression of nocturnal drizzle in stratocumulus polluted by haze. *Geophysical research letters*, 30(7).
- 9 Ackerman, A. S., Kirkpatrick, M. P., Stevens, D. E., and Toon, O. B., 2004: The impact of humidity above
10 stratiform clouds on indirect aerosol climate forcing. *Nature*, 432(7020), 1014-1017.
- 11 Albrecht, B.A., 1989: Aerosols, cloud microphysics, and fractional cloudiness. *Science*, 245(4923), 1227-1230.
- 12 Albrecht, B.A., Bretherton, C.S., Johnson, D., Schubert, W.H. and Frisch, A.S., 1995: The Atlantic stratocumulus
13 transition experiment—ASTEX. *Bulletin of the American Meteorological Society*, 76(6), 889-904.
- 14 Albrecht, B.A., 1993. Effects of precipitation on the thermodynamic structure of the trade wind boundary
15 layer. *Journal of Geophysical Research: Atmospheres*, 98(D4), 7327-7337.
- 16 Albrecht, B., V. Ghate, J. Mohrmann, R. Wood, et al., 2019: Cloud System Evolution in the Trades—CSET
17 Following the Evolution of Boundary Layer Cloud Systems with the NSF/NCAR GV. *Bull. Amer. Meteor.*
18 *Soc.*, 100, 93–121, doi: 10.1175/BAMS-D-17-0180.1.
- 19 Berner, A. H., C. S. Bretherton, R. Wood, and A. Muhlbauer, 2013: Marine boundary layer cloud regimes and POC
20 formation in an LES coupled to a bulk aerosol scheme. *Atmos. Chem. Phys.*, 13, 12549–12572,
21 <https://doi.org/10.5194/acp-13-12>
- 22 Blossey, P.N., Bretherton, C.S., Zhang, M., Cheng, A., Endo, S., Heus, T., Liu, Y., Lock, A.P., de Roode, S.R. and
23 Xu, K.M., 2013. Marine low cloud sensitivity to an idealized climate change: The CGILS LES
24 intercomparison. *Journal of Advances in Modeling Earth Systems*, 5(2), 234-258

1 Blossey, P. N., C. S. Bretherton, J. Mohrmann, 2021: Simulating observed cloud transitions in the northeast Pacific
2 during CSET. *Mon. Wea. Rev.*, 149(8), 2633-2658, <https://doi.org/10.1175/MWR-D-20-0328.1>

3 Bony, S. and Dufresne, J.L., 2005: Marine boundary layer clouds at the heart of tropical cloud feedback
4 uncertainties in climate models. *Geophysical Research Letters*, 32(20).

5 Bretherton, C. S., & Wyant, M. C., 1997: Moisture transport, lower-tropospheric stability, and decoupling of cloud-
6 topped boundary layers. *J. Atmos. Sci.*, 54 (1), 148-167.

7 Bretherton, C. S., S. K. Krueger, M. C. Wyant, P. Bechtold, E. Van Meijgaard, B. Stevens, and J. Teixeira, 1999: A
8 GCSS boundary-layer cloud model intercomparison study of the first ASTEX Lagrangian experiment. *Bound.-*
9 *Layer Meteor.*, **93**, 341–380,

10 Bretherton, C.S., Uttal, T., Fairall, C.W., Yuter, S.E., Weller, R.A., Baumgardner, D., Comstock, K., Wood, R. and
11 Raga, G.B., 2004: The EPIC 2001 stratocumulus study. *Bulletin of the American Meteorological Society*, 85(7),
12 967-978.

13 Bretherton, C. S., Blossey, P. N., & Uchida, J., 2007: Cloud droplet sedimentation, entrainment efficiency, and
14 subtropical stratocumulus albedo. *Geophysical research letters*, 34(3), L03813.

15 Bretherton, C. S., McCoy, I. L., Mohrmann, J., Wood, R., Ghate, V., Gettelman, A., Bardeen, C. G., Albrecht, B. A.,
16 & Zuidema, P. (2019). Cloud, Aerosol, and Boundary Layer Structure across the Northeast Pacific
17 Stratocumulus–Cumulus Transition as Observed during CSET. *Mon. Wea. Rev.*, 147(6), 2083–2103.
18 <https://doi.org/10.1175/MWR-D-18-0281.1>

19 Chen, R., Wood, R., Li, Z., Ferraro, R. and Chang, F.L., 2008: Studying the vertical variation of cloud droplet
20 effective radius using ship and space-borne remote sensing data. *Journal of Geophysical Research:*
21 *Atmospheres*, 113(D8).

22 Chin, M., P. Ginoux, S. Kinne, O. Torres, B. Holben, B. Duncan, R. Martin, J. Logan, A. Higurashi, and T.
23 Nakajima, 2002: Tropospheric aerosol optical thickness from the GOCART model and comparisons with
24 satellite and Sun photometer measurements. *J Atmos Sci*, 59-3, 461–483.

25 Comstock, K. K., Wood, R., Yuter, S. E., & Bretherton, C. S. (2004). Reflectivity and rain rate in and
26 below drizzling stratocumulus. *Quarterly Journal of the Royal Meteorological Society*, 130(603), 2891–2918.

27 Christensen, M.W., Jones, W.K. and Stier, P., 2020: Aerosols enhance cloud lifetime and brightness along the
28 stratus-to-cumulus transition. *Proceedings of the National Academy of Sciences*, 117(30), 17591-17598.

1 Diamond, M. S., Director, H. M., Eastman, R., Possner, A., & Wood, R., 2020: Substantial Cloud Brightening from
2 Shipping in Subtropical Low Clouds. *AGU Advances*, 1, e2019AV000111.
3 <https://doi.org/10.1029/2019AV000111>.

4 Doelling, D. R., M. Sun, L. T. Nguyen, M. L. Nordeen, C. O. Haney, D. F. Keyes, and P. E. Mlynczak, 2016:
5 Advances in geostationary-derived longwave fluxes for the CERES synoptic (SYN1deg) product. *J. Atmos.*
6 *Oceanic Technol.*, **33** (3), 503–521, doi:10.1175/JTECH-D-15-0147.1.

7 Eastman, R., & Wood, R., 2016: Factors controlling low-cloud evolution over the eastern subtropical oceans: A
8 Lagrangian perspective using the A-Train satellites. *Journal of the Atmospheric Sciences*, 73(1), 331-351.

9 Eastman, R., Wood, R. & O, K-T., 2017: The subtropical stratocumulus-topped planetary boundary layer: A
10 climatology and the Lagrangian evolution. *J. Atmos. Sci.*, 74, 2633-2656. <https://doi.org/10.1175/JAS-D-16->
11 0336.1

12 Eastman, R., Lebsock, M., & Wood, R., 2019: Warm Rain Rates from AMSR-E 89-GHz Brightness Temperatures
13 Trained Using CloudSat Rain-Rate Observations. *Journal of Atmospheric and Oceanic Technology*, 36(6),
14 1033–1051.

15 Feingold, G. and Kreidenweis, S. M.: Cloud processing of aerosol as modeled by a large eddy simulation with
16 coupled microphysics and aqueous chemistry, *J. Geophys. Res.*, 107, 4687, doi:10.1029/2002JD002054, 2002.

17 Gelaro, R., McCarty, W., Suárez, M. J., Todling, R., Molod, A., Takacs, L., et al., 2017: The modern-era
18 retrospective analysis for research and applications, version 2 (MERRA-2). *J. Clim.*, 30(14), 5419-5454.

19 George, R. C., and R. Wood, 2010: Subseasonal variability of low cloud radiative properties over the southeast
20 Pacific Ocean. *Atmos. Chem. Phys.*, 10, 4047–4063, <https://doi.org/10.5194/acp-10-4047-2010>.

21 Glassmeier, F., Hoffmann, F., Johnson, J. S., Yamaguchi, T., Carslaw, K. S., & Feingold, G., 2021: 900 Aerosol-
22 cloud-climate cooling overestimated by ship-track data. *Science*, 371(6528), 485–489.
23 <https://doi.org/10.1126/science.abd3980>.

24 Gong, S., 2003: A parameterization of sea-salt aerosol source function for sub- and super-micron particles. *Global*
25 *Biogeochemical Cycles*, 17(4), 1097.

26 Goren, T., Kazil, J., Hoffmann, F., Yamaguchi, T., & Feingold, G., 2019: Anthropogenic Air Pollution Delays
27 Marine Stratocumulus Breakup to Open Cells. *Geophysical Research Letters*, 46(23), 14135–14144.
28 <https://doi.org/10.1029/2019GL085412>.

1 Grainger, R. G., 2012: Some useful formulae for aerosol size distributions and optical properties. *Lect. Notes*
2 *(University of Oxford)*, 12-3.

3 Grosvenor, D. P., et al., 2018: Remote Sensing of Droplet Number Concentration in Warm Clouds: A Review of the
4 Current State of Knowledge and Perspectives. *Reviews of Geophysics*, 56(2), 409–453.
5 <https://doi.org/10.1029/2017RG000593>.

6 Gryspeerdt, E., Goren, T., Sourdeval, O., Quaas, J., Mülmenstädt, J., Dipu, S., Unglaub, C., Gettelman, A., and
7 Christensen, M., 2019: Constraining the aerosol influence on cloud liquid water path, *Atmos. Chem. Phys.*, 19,
8 5331–5347.

9 Hannay, C., Williamson, D.L., Hack, J.J., Kiehl, J.T., Olson, J.G., Klein, S.A., Bretherton, C.S. and Köhler, M.,
10 2009: Evaluation of forecasted southeast Pacific stratocumulus in the NCAR, GFDL, and ECMWF
11 models. *Journal of Climate*, 22(11), 2871-2889.

12 Hersbach, H., and Coauthors, 2020: The ERA5 global reanalysis. *Quart. J. Roy. Meteor. Soc.*, **146 (730)**, 1999–
13 2049, doi:10.1002/qj.3803.

14 Hoffmann, F., Glassmeier, F., Yamaguchi, T., & Feingold, G., 2020: Liquid Water Path Steady States in
15 Stratocumulus: Insights from Process-Level Emulation and Mixed-Layer Theory. *Journal of the Atmospheric*
16 *Sciences*, 77(6), 2203–2215. <https://doi.org/10.1175/JAS-D-19-0241.1>

17 IPCC, 2013: *Climate Change 2013: The Physical Science Basis*. T. F. Stocker et al., Eds., Cambridge University
18 Press, 1535 pp.

19 Kawanishi, T., Sezai, T., Ito, Y., Imaoka, K., Takeshima, T., Ishido, Y., Shibata, A., Miura, M., Inahata, H. and
20 Spencer, R.W., 2003: The Advanced Microwave Scanning Radiometer for the Earth Observing System
21 (AMSR-E), NASDA's contribution to the EOS for global energy and water cycle studies. *IEEE Transactions on*
22 *Geoscience and Remote Sensing*, 41(2), 184-194.

23 Khairoutdinov, M. F., and D. A. Randall, 2003: Cloud resolving modeling of the ARM summer 1997 IOP: Model
24 formulation, results, uncertainties, and sensitivities. *J. Atmos. Sci.*, 60 (4), 607–625, doi:10.1175/1520-
25 0469(2003)060<0607:CRMOTA>2.0.CO;2.

26 Kuan-Ting O, Wood, R., & Bretherton, C. S., 2018: Ultraclean Layers and Optically Thin Clouds in the
27 Stratocumulus-to-Cumulus Transition. Part II: Depletion of Cloud Droplets and Cloud Condensation Nuclei

1 through Collision–Coalescence. *Journal of the Atmospheric Sciences*, 75(5), 1653–1673.
2 <https://doi.org/10.1175/JAS-D-17-0218.1>

3 Platnick, S., & Twomey, S., 1994: Determining the Susceptibility of Cloud Albedo to Changes in Droplet
4 Concentration with the Advanced Very High-Resolution Radiometer. *Journal of Applied Meteorology*, 33(3),
5 334–347.[https://doi.org/10.1175/1520-0450\(1994\)033<0334:DTSOCA>2.0.CO;2](https://doi.org/10.1175/1520-0450(1994)033<0334:DTSOCA>2.0.CO;2).

6 Krueger, S. K., McLean, G. T., & Fu, Q., 1995: Numerical simulation of the stratus-to-cumulus transition in the
7 subtropical marine boundary layer. part I: Boundary-layer structure. *J. Atmos. Sci.*, 52 (16), 2839-2850.

8 Kubar, T.L., Stephens, G.L., Lebsock, M., Larson, V.E. and Bogenschutz, P.A., 2015: Regional assessments of low
9 clouds against large-scale stability in CAM5 and CAM-CLUBB using MODIS and ERA-Interim reanalysis
10 data. *Journal of Climate*, 28(4), 1685-1706.

11 Kubar, T. L., Xie, F., Ao, C. O., & Adhikari, L. (2020). An assessment of PBL heights and low cloud profiles in
12 CAM5 and CAM5-CLUBB over the Southeast Pacific using satellite observations. *Geophysical Research*
13 *Letters*, 47(2), e2019GL084498.

14 Lin, J.L., Qian, T. and Shinoda, T., 2014: Stratocumulus clouds in Southeastern Pacific simulated by eight CMIP5–
15 CFMIP global climate models. *Journal of Climate*, 27(8), 3000-3022

16 Masunaga, H., T. Y. Nakajima, T. Nakajima, M. Kachi, and K. Suzuki (2002b), Physical properties of maritime low
17 clouds as retrieved by combined use of TRMM Microwave Imager and Visible/Infrared Scanner: 2.
18 Climatology of warm clouds and rain, *J. Geophys. Res.*, **107**(D19), 4367, doi:10.1029/2001JD001269.

19 Minnis, P., and Coauthors, 2008: Near-real time cloud retrievals from operational and research meteorological
20 satellites. *Remote Sensing of Clouds and the Atmosphere XIII*, International Society for Optics and Photonics,
21 Vol. 7107, 710703, doi:10.1117/12.800344.

22 Mlawer, E.J., Taubman, S.J., Brown, P.D., Iacono, M.J. and Clough, S.A., 1997: Radiative transfer for
23 inhomogeneous atmospheres: RRTM, a validated correlated-k model for the longwave. *Journal of Geophysical*
24 *Research: Atmospheres*, 102(D14), 16663-16682.

25 Mohrmann, J., C. S. Bretherton, I. L. McCoy, J. McGibbon, and R. Wood, 2019: Lagrangian evolution of the
26 Northeast Pacific marine boundary layer structure and cloud during CSET. *Mon. Wea. Rev.*, 147, 4681–4700,
27 DOI: 10.1175/MWR-D-19-0053.1.

1 Morrison, H.C.J.A., Curry, J.A. and Khvorostyanov, V.I., 2005. A new double-moment microphysics
2 parameterization for application in cloud and climate models. Part I: Description. *Journal of the atmospheric*
3 *sciences*, 62(6), 1665-1677.

4 Neale, R. B., and Coauthors, 2010: Description of the NCAR Community Atmosphere Model (CAM5.0). NCAR
5 Tech. Note NCAR/TN-4861STR, 268 pp.,
6 www.cesm.ucar.edu/models/cesm1.1/cam/docs/description/cam5_desc.pdf.

7 Sandu, I., Brenguier, J.L., Geoffroy, O., Thoueron, O. and Masson, V., 2008: Aerosol impacts on the diurnal cycle of
8 marine stratocumulus. *Journal of Atmospheric Sciences*, 65(8), 2705-2718.

9 Sandu, I. and Stevens, B., 2011: On the factors modulating the stratocumulus to cumulus transitions. *Journal of*
10 *Atmospheric Sciences*, 68(9), 1865-1881.

11 Seifert, A., and T. Heus, 2013: Large-eddy simulation of organized precipitating trade wind cumulus clouds. *Atmos.*
12 *Chem. Phys.*, 13, 5631–5645.

13 Stevens, B. and Seifert, A., 2008. Understanding macrophysical outcomes of microphysical choices in simulations
14 of shallow cumulus convection. *Journal of the Meteorological Society of Japan. Ser. II*, 86, pp.143-162.

15 Slingo, A., 1990: Sensitivity of the Earth's radiation budget to changes in low clouds. *Nature*, 343(6253), 49-51.

16 Stephens, G.L., Paltridge, G.W. and Platt, C.M.R., 1978: Radiation profiles in extended water clouds. III:
17 Observations. *Journal of Atmospheric Sciences*, 35(11), 2133-2141.

18 Stevens, B., Feingold, G., 2009: Untangling aerosol effects on clouds and precipitation in a buffered
19 system. *Nature* **461**, 607–613. <https://doi.org/10.1038/nature08281>

20 Twomey, S., 1977: The Influence of Pollution on the Shortwave Albedo of Clouds. *J. Atmos. Sci.*, 34, 1149–1152.
21 [https://doi.org/10.1175/1520-0469\(1977\)034<1149:TlOPOT>2.0.CO;2](https://doi.org/10.1175/1520-0469(1977)034<1149:TlOPOT>2.0.CO;2).

22 Teixeira, J., Cardoso, S., Bonazzola, M., Cole, J., DelGenio, A., DeMott, C., Franklin, C., Hannay, C., Jakob, C.,
23 Jiao, Y. and Karlsson, J., 2011: Tropical and subtropical cloud transitions in weather and climate prediction
24 models: The GCSS/WGNE Pacific Cross-Section Intercomparison (GPCI). *Journal of Climate*, 24(20), 5223-
25 5256.

26 Toll, V., Christensen, M., Gassó, S., & Bellouin, N., 2017: Volcano and ship tracks indicate excessive aerosol-
27 induced cloud water increases in a climate model. *Geophysical Research Letters*, 44, 12,492–12,500.
28 <https://doi.org/10.1002/2017GL075280>.

1 Van der Dussen, J.J., De Roode, S.R. and Siebesma, A.P., 2016: How large-scale subsidence affects stratocumulus
2 transitions. *Atmospheric Chemistry and Physics*, 16(2), 691-701

3 Wentz, F., K. Hilburn, and D. Smith, 2012: Remote Sensing Systems DMSP SSM/I Daily Environmental Suite on
4 0.25 deg grid, Version 7. Remote Sensing Systems, Santa Rosa, CA, available at:
5 <http://www.remss.com/missions/ssmi/>.

6 Williams, A. S., & Igel, A. L., 2021: Cloud Top Radiative Cooling Rate Drives Non-Precipitating Stratiform Cloud
7 Responses to Aerosol Concentration. *Geophysical Research Letters*, 48(18), e2021GL094740.
8 <https://doi.org/10.1029/2021GL094740>.

9 Wood, R., 2007: Cancellation of Aerosol Indirect Effects in Marine Stratocumulus through Cloud Thinning. *J.*
10 *Atmos. Sci.*, 64, 2657–2669. <https://doi.org/10.1175/JAS3942.1>.

11 Wood, R., Kubar, T.L. and Hartmann, D.L., 2009: Understanding the importance of microphysics and macrophysics
12 for warm rain in marine low clouds. Part II: Heuristic models of rain formation. *Journal of the Atmospheric*
13 *Sciences*, 66(10), 2973-2990.

14 Wood, R., Bretherton, C.S., Leon, D., Clarke, A.D., Zuidema, P., Allen, G. and Coe, H., 2011: An aircraft case
15 study of the spatial transition from closed to open mesoscale cellular convection over the Southeast
16 Pacific. *Atmospheric Chemistry and Physics*, 11(5), 2341-2370.

17 Wood, R., 2012: Stratocumulus clouds. *Monthly Weather Review*, 140(8), 2373-2423.

18 Wood, R., O, K.T., Bretherton, C.S., Mohrmann, J., Albrecht, B.A., Zuidema, P., Ghate, V., Schwartz, C., Eloranta,
19 E., Glienke, S. and Shaw, R.A., 2018: Ultraclean layers and optically thin clouds in the stratocumulus to-
20 cumulus transition. Part I: Observations. *J. Atmos. Sci.*, 75 (5), 1631–1652, doi:10.1175/JAS-D-17-0213.1.

21 Wood, R., 2021: Assessing the potential efficacy of marine cloud brightening for cooling Earth using a simple
22 heuristic model, *Atmos. Chem. Phys.*, 21, 14507–14533.

23 Wyant, M.C., Bretherton, C.S., Rand, H.A. and Stevens, D.E., 1997: Numerical simulations and a conceptual model
24 of the stratocumulus to trade cumulus transition. *Journal of Atmospheric Sciences*, 54(1), 168-192.

25 Xue, H., Feingold, G., & Stevens, B., 2008: Aerosol effects on clouds, precipitation, and the organization of shallow
26 cumulus convection. *Journal of the Atmospheric Sciences*, 65(2), 392-406.

27 Yamaguchi, T. and Feingold, G., 2015: On the relationship between open cellular convective cloud patterns and the
28 spatial distribution of precipitation. *Atmospheric Chemistry and Physics*, 15(3), 1237-1251.

1 Yamaguchi, T., Feingold, G. and Kazil, J., 2017: Stratocumulus to cumulus transition by drizzle. *Journal of*
2 *Advances in Modeling Earth Systems*, 9(6), 2333-2349.

3 Zelinka, M.D., Randall, D.A., Webb, M.J. and Klein, S.A., 2017: Clearing clouds of uncertainty. *Nature Climate*
4 *Change*, 7(10), 674-678.

5 Zhou, X., Kollias, P. and Lewis, E.R., 2015: Clouds, precipitation, and marine boundary layer structure during the
6 MAGIC field campaign. *Journal of Climate*, 28(6), 2420-2442.

7 MERRA2 FAQ webpage: <https://gmao.gsfc.nasa.gov/reanalysis/MERRA-2/FAQ/>, valid as of 5/20/2022.

8

1 **Figure Captions**

2 Figure 1. Selected CSET Lagrangian trajectories (filled markers) and flight paths (westward solid
3 cyan lines, eastward dashed cyan lines) for the a) L06 and b) L10 cases used in this study. The
4 filled markers' shades show the evolution in CERES low cloud cover along the trajectories. In the
5 background map, shaded contours, black contours, and vectors show the ERA5 SST, surface
6 pressure, and 10m wind speed, respectively, averaged for the periods a) 17-20 July 2015 and b)
7 27-30 July 2015.

8 Figure 2. Time-height evolution of corrected MERRA2 N_a for the a) L06 and b) L10 cases. The
9 superimposed thin vertical rectangles at about days 0.75 and 2.75 show the aircraft measurements
10 of N_a for reference.

11 Figure 3. Left panels: time series for L06 of observed and modeled domain-averaged a) MBL-
12 average total aerosol number concentration ($\langle N_a \rangle$), b) MBL-average cloud droplet number
13 concentration ($\langle N_c \rangle$), and c) the shortwave cloud radiative effect (SW CRE, calculated as the all-
14 sky minus clear-sky net SW at TOA). Right panels: select MBL-average budget tendencies for N_a
15 due to d) cloud-top entrainment of lower FT air, e) MBL-averaged scavenging, and f) surface
16 fluxes.

17 Figure 4. Vertical profiles of the observed and modeled domain-averaged N_a and N_c at the time of
18 the a) westward and b) return flight observations for the L06 case. c&d) as in (a&b), but for relative
19 humidity (RH).

20 Figure 5. Macrophysical cloud properties for the L06 case from the simulations and observations.
21 Time series of domain-averaged a) low cloud cover (LCC), b) accumulated precipitation, c)
22 inversion height (Z_{inv}), d) cloud liquid water path (LWP), e) entrainment rate (w_e), and f) outgoing
23 longwave radiation (OLR).

24 Figure 6. As in Figure 3, but for the L10 case.

25 Figure 7. As in Figure 4, but for the L10 case.

26 Figure 8. As in Figure 5, but for the L10 case.

27 Figure 9. Microphysical and macrophysical variables as a function of $\langle N_c \rangle$ for the L06 (circles)
28 and L10 (squares) cases, from both the simulations and selected observations. Variables on the y-

1 axis are a) the short-wave cloud radiative effect (SW CRE), b) cloud LWP, c) LCC, d) surface
 2 precipitation, e) τ_c , f) r_e , g) Z_{inv} , and h) w_e . Each colored point shows results for one LES run
 3 averaged over the whole day-time period of the run. Observed values are plotted as black or gray
 4 circles for L06 and black or gray squares for L10 case. Here, the observed values of $\langle N_c \rangle$ are from
 5 GOES and the observed or reanalysis values of parameters are from sources as given in the upper-
 6 right corner of each panel.

7 Figure 10. Time-height evolution of a&b) w'^2 , c&d) cloud fraction (CF) and precipitation flux,
 8 and e&f) N_a . The x-axis is time in fraction of a day relative to the time of the SCT. G&h) The
 9 vertical profiles of N_a are shown at several times near the time of the SCT. For each time, the
 10 shaded area between the two lines shows the 5th and 95th percentile range in the variable's
 11 probability distribution function (PDF). The results are for two LES runs: L06 MERRA-LD (left
 12 panels) and L10 250-60-LD (right panels).

13 Figure 11. Left panels: snapshots of a) surface precipitation, and b) cloud LWP for the L06
 14 MERRA-LD run at a time close to the SCT, day 1.875 (relative to the run start). Right panels: y-z
 15 cross-sections of c) N_a and d) N_c , with contours of rain mass or q_r ($1e-4, 1e-3 \text{ kg kg}^{-1}$) and cloud
 16 liquid mass or q_c ($1e-5, 1e-4, 1e-3 \text{ kg kg}^{-1}$). Cross-sections are at $x = 8 \text{ km}$ (black lines in the left
 17 panels).

18 Figure 12. As in Figure 11, but for L10 250-60-LD and for x-z cross-sections at $y = 23 \text{ km}$ (black
 19 lines on left panels). Here, the data are for day 3.375 relative to the run start.

20 Figure 13. Upper panels: change in cloudy-sky albedo (ΔA_c) as a function of the ratio of the
 21 perturbed to baseline cloud droplet number concentration ($r_N = \frac{N_{c2}}{N_{c1}}$) for a) L06 and b) L10. Lower
 22 panels: change in the cloud radiative effect (ΔR) as a function of r_N for c) L06 and d) L10. Each
 23 point shows the variables for a pair of LES runs with values averaged over the whole day-time
 24 period of the run. The filled circles show the total change in A_c and R between the two LES runs.
 25 The square, diamond, triangle, and plus markers, respectively, show the effects of changes in N_c ,
 26 LWP, CF, and the residual (CDNC + LWP + CF - Total). The markers for N_c , LWP, CF, and
 27 residual show the results of step 3, whereas the endpoints of bars show steps 1 and 2 of the
 28 calculations described in the text.

1 Figure 14. Upper panels: ratio of the perturbed to baseline cloud fraction ($r_C = \frac{C_2}{C_1}$) as a function of
2 the ratio of the perturbed to baseline cloud droplet number concentration ($r_N = \frac{N_{c2}}{N_{c1}}$) for the a) L06
3 and b) L10 cases. Lower panels: r_N as a function of the ratio of the perturbed to baseline liquid
4 water path ($r_L = \frac{L_2}{L_1}$) for the c) L06 and d) L10 cases. Each point shows the ratio between a pair of
5 LES runs with values averaged over the whole day-time period of the run.

6 Figure A1. Linear regression in log-log space between N_a from all CSET flights and N_a derived
7 from collocated MERRA2 data.

8 Figure S1. Snapshots of cloud LWP for the L06, 40-40-LD run on days a) 0.6, b) 1.6, c) 2.6 and
9 d) 3.6 following the start of the simulation. e-h) As in a-d, but for the L10, 250-60 run.

10 Figure S2. a) Time series of observed and modeled domain-averaged, MBL-averaged $\langle N_c \rangle$ for
11 this study's L06 40-40-LD run and for the L06 Lx29 run from B21. b) Time-height evolution of
12 domain-averaged cloud fraction for this study's L06 40-40-LD run. c) As in b, but for the L06
13 Lx29 run from B21. d-f) As in a-c, but for this study's L10 250-60-LD run and the L10 Lx29 run
14 from B21.

15 Figure S3. a-d) Probability distribution functions of cloud LWP at four times for L06, MERRA
16 and MERRA-LD runs. The dots show precipitation in bins of LWP, and the boxes on the upper-
17 left corner of each panel show domain-averaged LWP for MERRA (first value) and MERRA-LD
18 (second value). Each panel shows data averaged for a period of 1 hour. e-h) as in a-d, but for $\langle N_c \rangle$.
19 i-l) Snapshots of cloud LWP at four times for MERRA run. m-p) as in i-l, but for MERRA-LD
20 run.

21 Fig. S4. As in Fig. S3, but for 250-60 and 250-60-LD runs.

22 Fig. S5. Time series of a) LCC, b) cloud LWP, c) 95th percentile cloud LWP $\langle N_c \rangle^{-1}$, and d) 95th
23 percentile surface precipitation for all the runs with clear SCT. The x-axis is time (in units of
24 day) with SCT selected as 0.

25

1 Table 1. A description of LES runs performed in this study.
 2

Run name	Case	Domain size (km)	Initial MBL N_a (mg^{-1})	FT N_a (mg^{-1})
40-40	L06	9.6×9.6	40	40
40-40to150	L06	9.6×9.6	40	Initial: 40 gradual increase to: 150
150-40	L06	9.6×9.6	150	40
40-150	L06	9.6×9.6	40	150
MERRA	L06	9.6×9.6	MERRA (103)*	MERRA (68)**
MERRAx3	L06	9.6×9.6	MERRAx3 (309)*	MERRA (68)**
40-40-LD	L06	25.6×25.6	40	40
MERRA-LD	L06	25.6×25.6	MERRA (103)*	MERRA (68)**
70-60	L10	9.6×9.6	70	60
110-60	L10	9.6×9.6	110	60
250-60	L10	9.6×9.6	250	60
250-200	L10	9.6×9.6	250	200
MERRA	L10	9.6×9.6	MERRA (215)*	MERRA (270)**
MERRAx3	L10	9.6×9.6	MERRAx3 (645)*	MERRA (270)**
250-60-LD	L10	25.6×25.6	250	60
70-60-LD	L10	25.6×25.6	70	60

3 * Initial MBL-averaged N_a based on MERRA data

4 ** Time-mean FT value of N_a right above the inversion from MERRA data

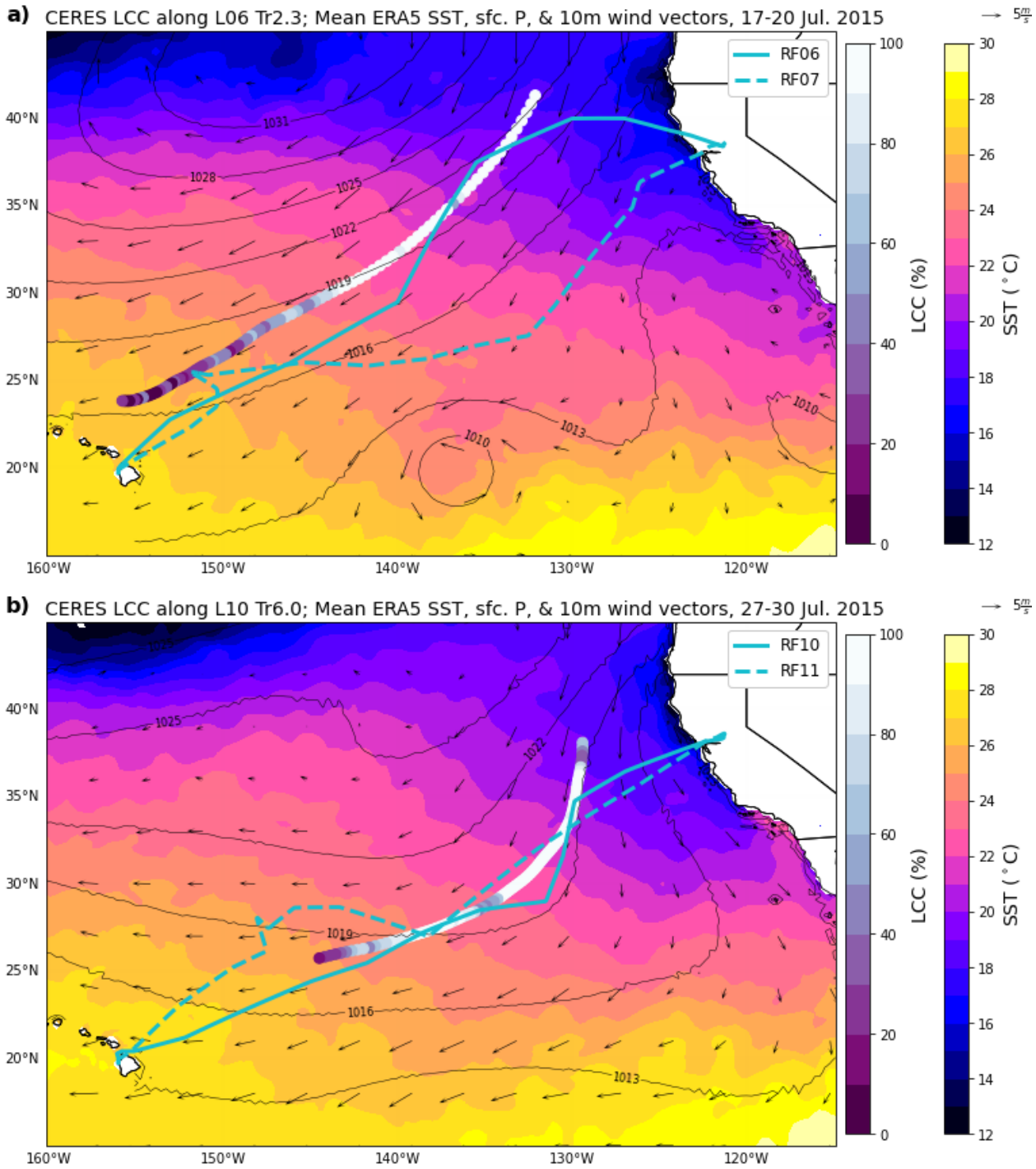
5

1 Table A1. Various aerosol properties for different tracers available in MERRA2 data. This table is compiled based on
 2 the results of Chin et al. (2002) and MERRA2 FAQ webpage.

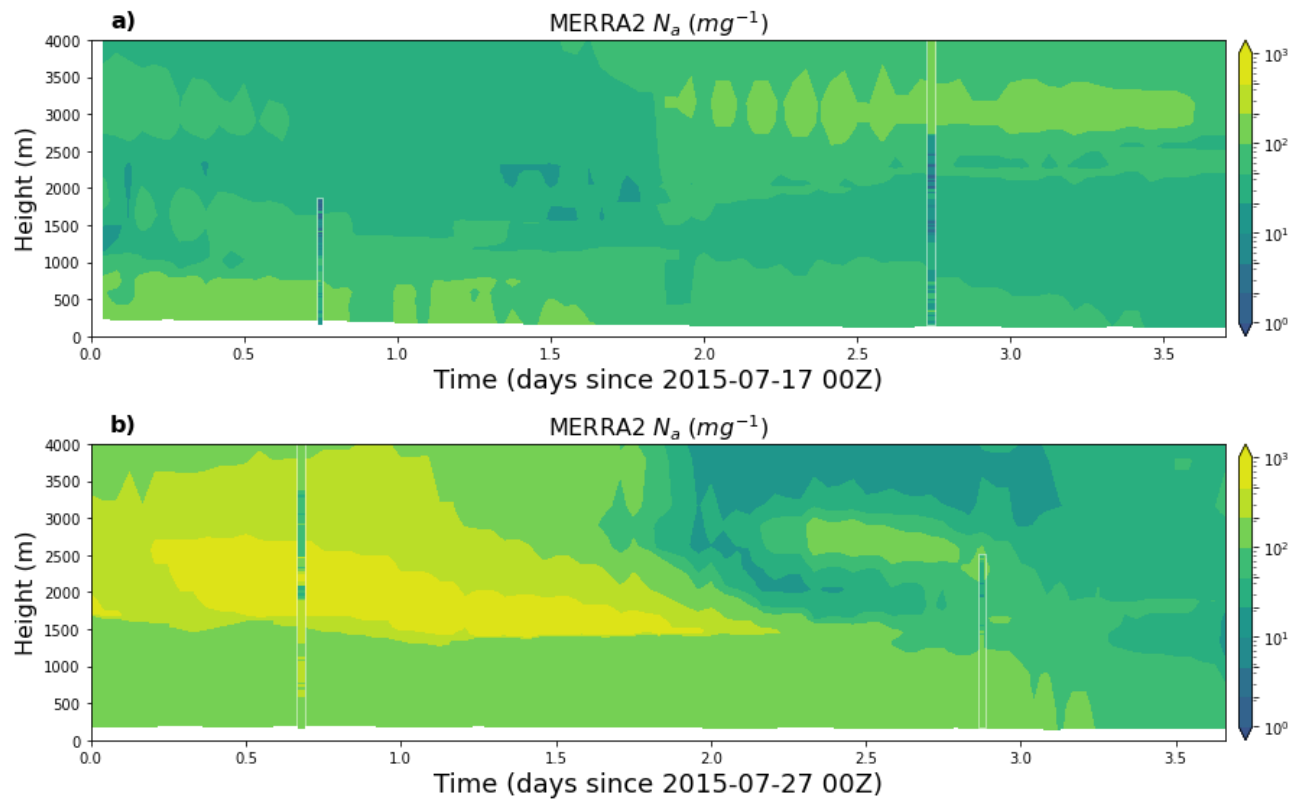
Aerosol tracer	Size distribution	Density (kg m ⁻³)	Modal radius (μm)	Effective radius (μm)	Lower radius (μm)	Upper radius (μm)	mass weight	Geometric standard deviation (μm)
OC, hydrophilic	Lognormal	1800	0.0212	---	0.1	0.3	---	2.20
OC, hydrophobic	Lognormal	1800	0.0212	---	0.1	0.3	---	2.20
BC, hydrophilic	Lognormal	1800	0.0118	---	0.1	0.3	---	2.00
BC, hydrophobic	Lognormal	1800	0.0118	---	0.1	0.3	---	2.00
Sulfate	Lognormal	1700	0.0695	---	0.1	0.3	---	2.03
Dust, 1	Power special	2500	0.220	0.73	0.10	0.18	0.009	2.00
					0.18	0.3	0.081	
					0.3	0.6	0.234	
					0.6	1.0	0.676	
Dust, 2	Power	2650	0.421	1.4	1.0	1.8	---	2.00
Dust, 3	Power	2650	0.7220	2.4	1.8	3.0	---	2.00
Dust, 4	Power	2650	1.3540	4.5	3.0	6.0	---	2.00
Dust, 5	Power	2650	2.4068	8.0	6.0	10.0	---	2.00
Sea Salt, 1	Modified Gamma	2200	0.023	0.079	0.03	0.1	---	2.03
Sea Salt, 2	Modified Gamma	2200	0.090	0.316	0.1	0.5	---	2.03
Sea Salt, 3	Modified Gamma	2200	0.090	1.119	0.5	1.5	---	2.03
Sea Salt, 4	Modified Gamma	2200	0.805	2.818	1.5	5.0	---	2.03
Sea Salt, 5	Modified Gamma	2200	2.219	7.772	5.0	10.0	---	2.03

3

4

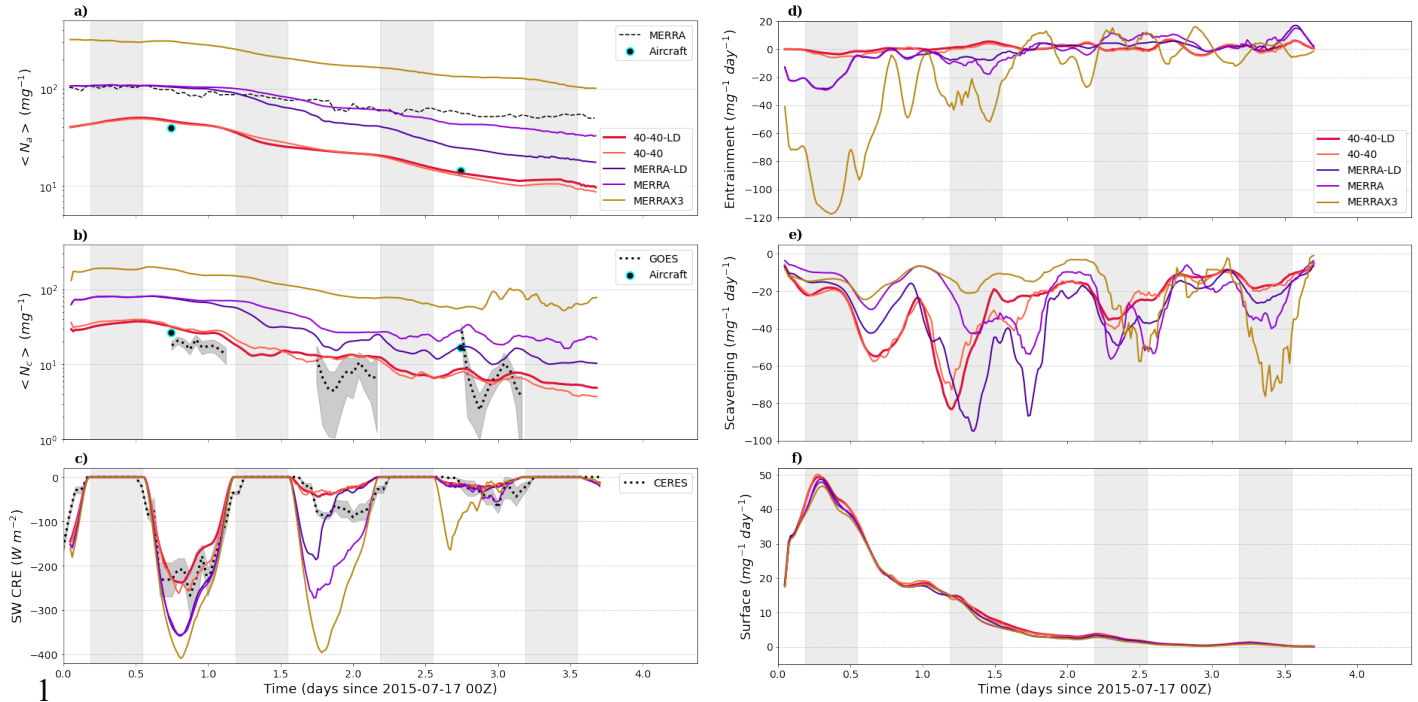


1
 2 Figure 1. Selected CSET Lagrangian trajectories (filled markers) and flight paths (westward solid cyan lines, eastward
 3 dashed cyan lines) for the a) L06 and b) L10 cases used in this study. The filled markers' shades show the evolution
 4 in CERES low cloud cover along the trajectories. In the background map, shaded contours, black contours, and vectors
 5 show the ERA5 SST, surface pressure, and 10m wind speed, respectively, averaged for the periods a) 17-20 July 2015
 6 and b) 27-30 July 2015.



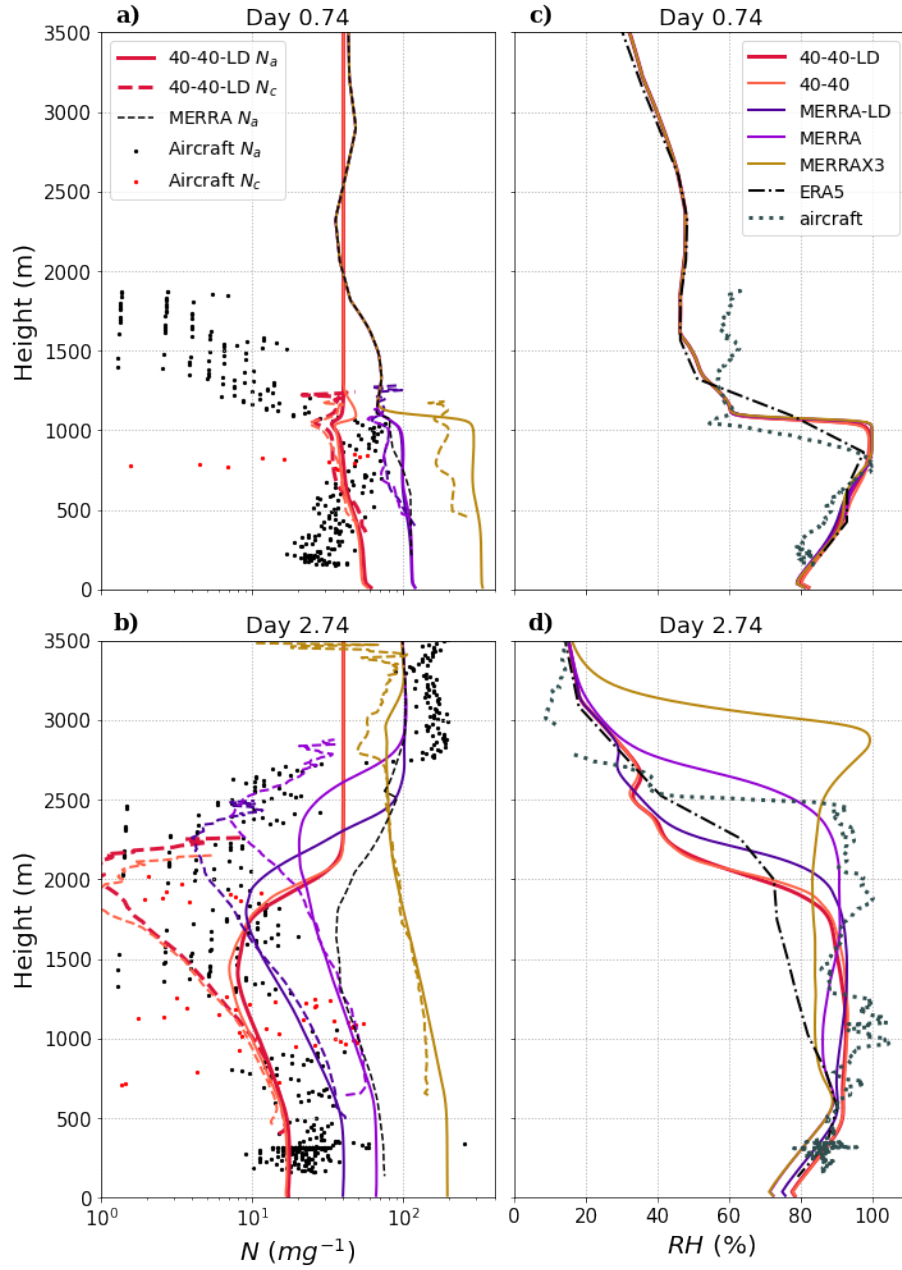
1
 2 Figure 2. Time-height evolution of corrected MERRA2 N_a for the a) L06 and b) L10 cases. The superimposed thin
 3 vertical rectangles at about days 0.75 and 2.75 show the aircraft measurements of N_a for reference.

4



1
 2 Figure 3. Left panels: time series for L06 of observed and modeled domain-averaged a) MBL-average total aerosol
 3 number concentration ($\langle N_a \rangle$), b) MBL-average cloud droplet number concentration ($\langle N_c \rangle$), and c) the shortwave
 4 cloud radiative effect (SW CRE, calculated as the all-sky minus clear-sky net SW at TOA). Right panels: select MBL-
 5 average budget tendencies for N_a due to d) cloud-top entrainment of lower FT air, e) MBL-averaged scavenging, and
 6 f) surface fluxes.

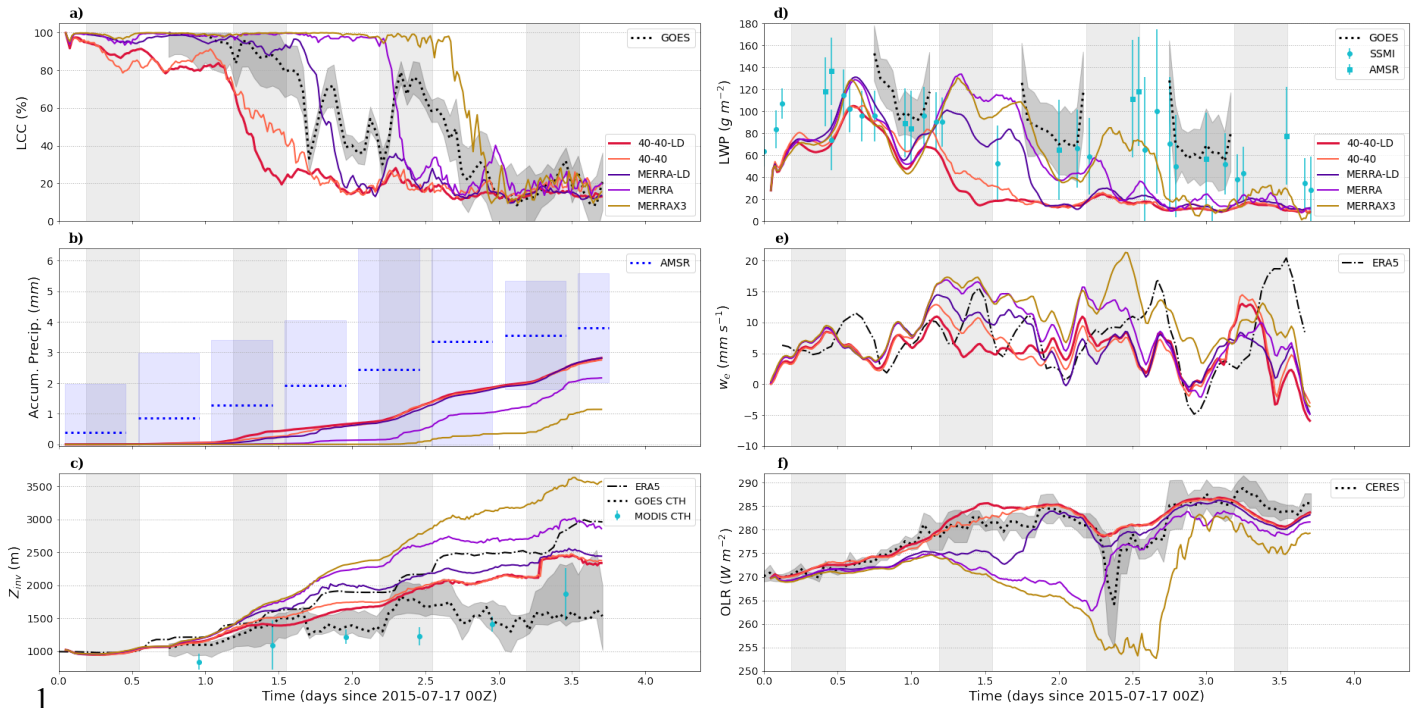
7



1

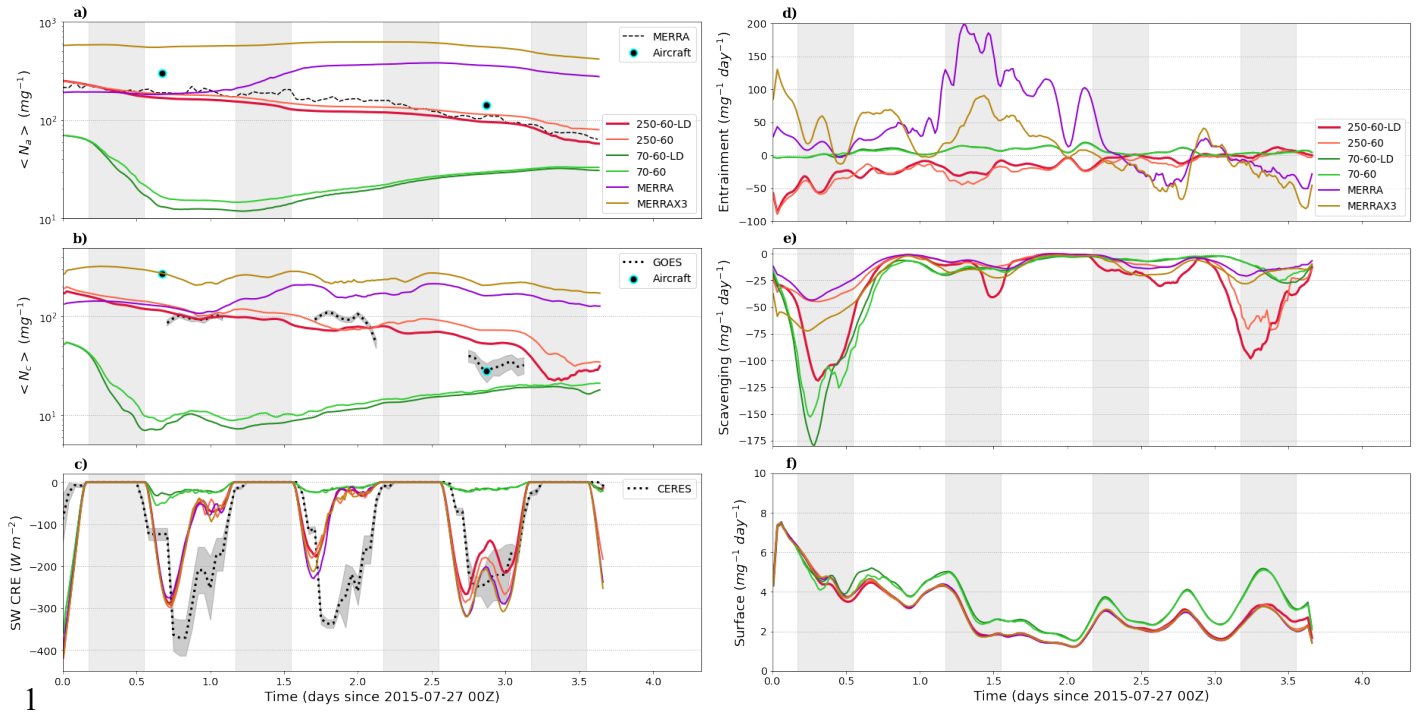
2 Figure 4. Vertical profiles of the observed and modeled domain-averaged N_a and N_c at the time of the a) westward and
 3 b) return flight observations for the L06 case. c&d) as in (a&b), but for relative humidity (RH).

4



1
2
3
4
5

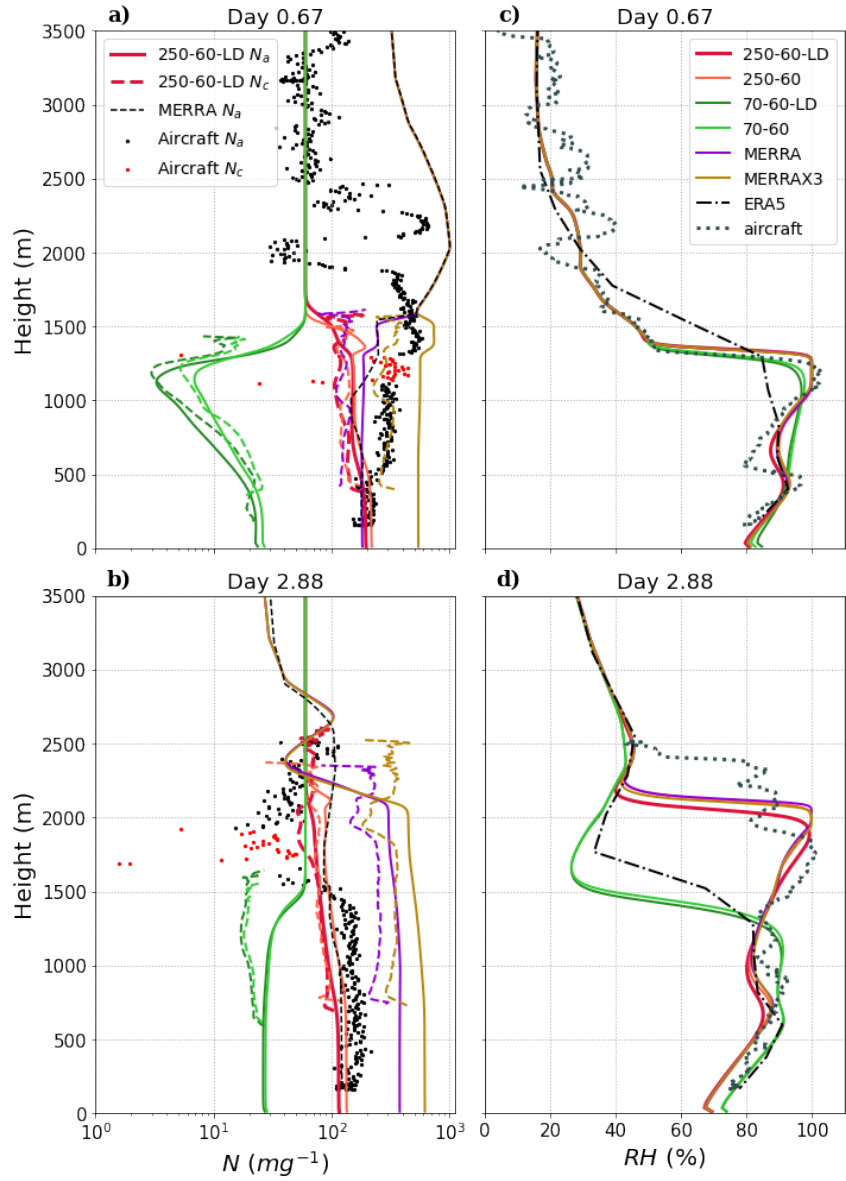
Figure 5. Macrophysical cloud properties for the L06 case from the simulations and observations. Time series of domain-averaged a) low cloud cover (LCC), b) accumulated precipitation, c) inversion height (Z_{inv}), d) cloud liquid water path (LWP), e) entrainment rate (w_e), and f) outgoing longwave radiation (OLR).



1

2 Figure 6. As in Figure 3, but for the L10 case.

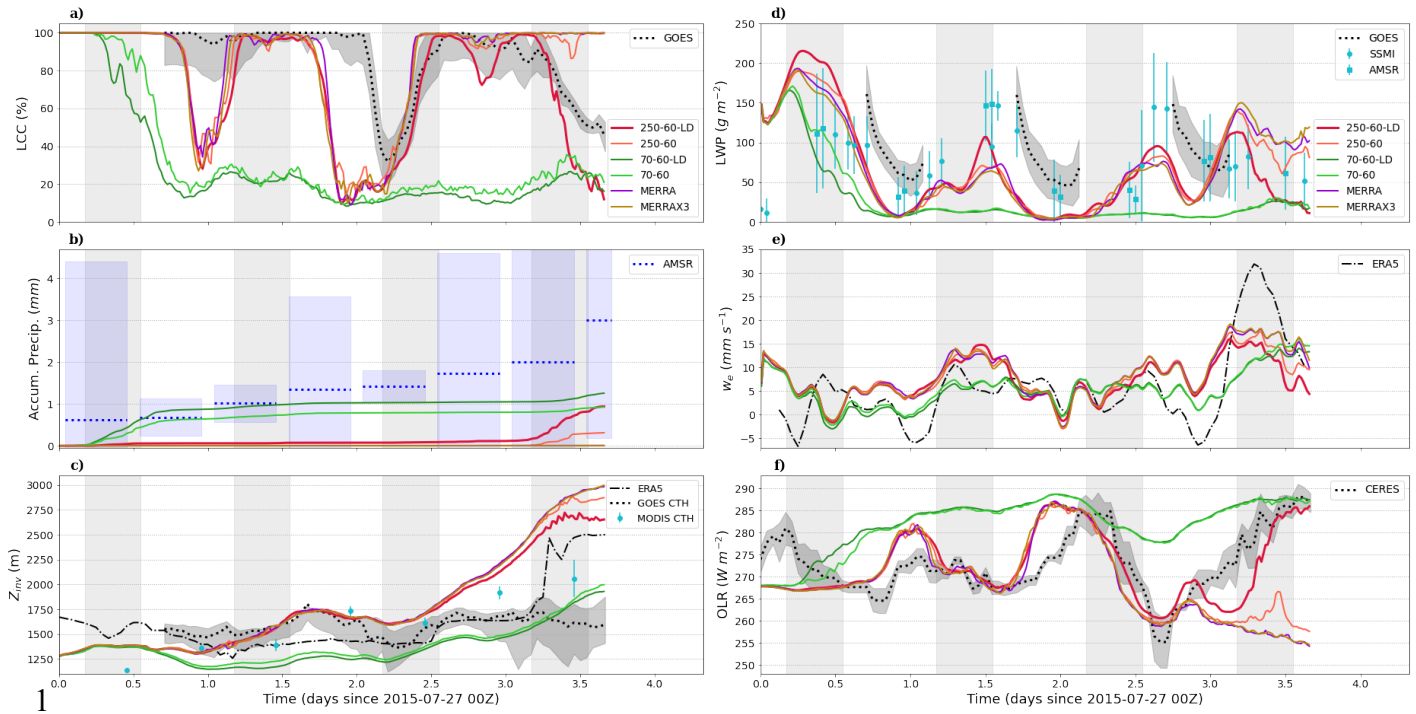
3



1

2 Figure 7. As in Figure 4, but for the L10 case.

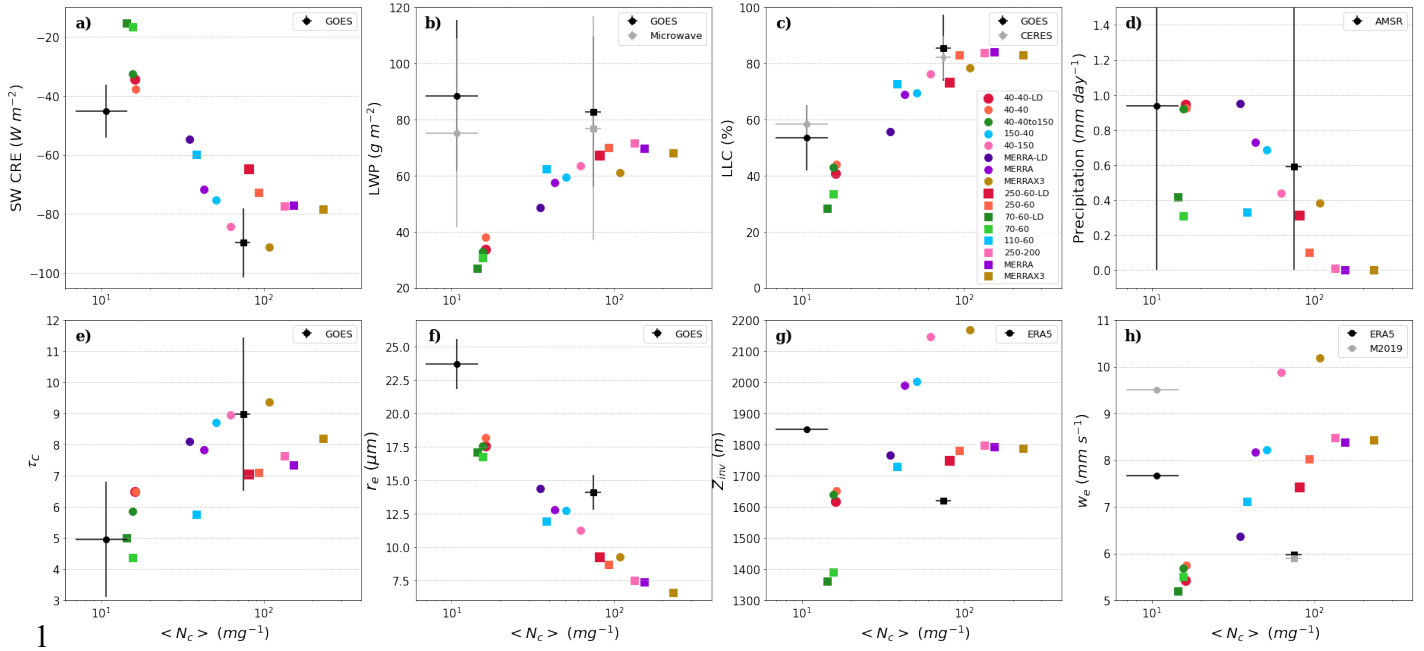
3



1

2 Figure 8. As in Figure 5, but for the L10 case.

3



1

2

3

4

5

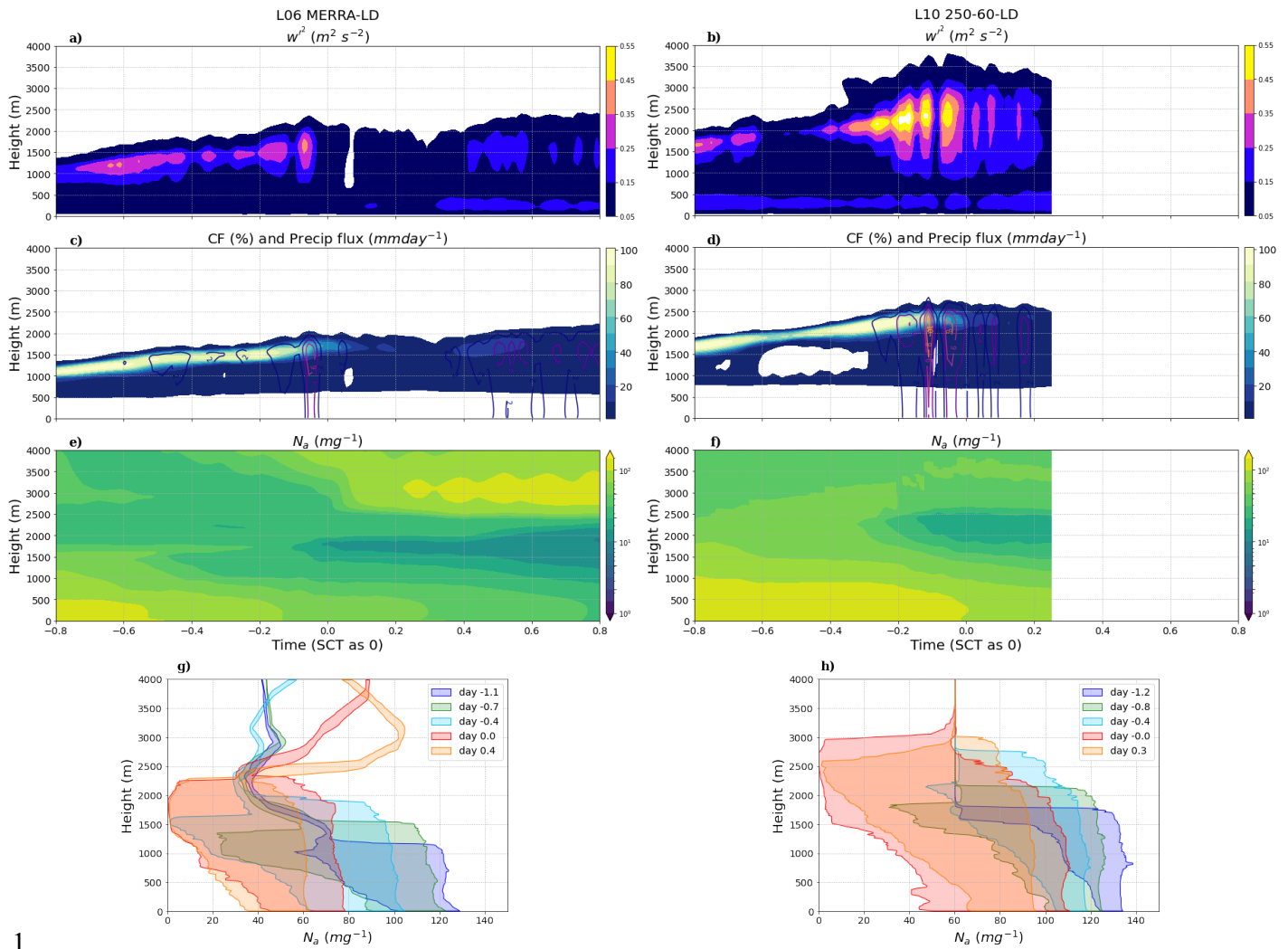
6

7

8

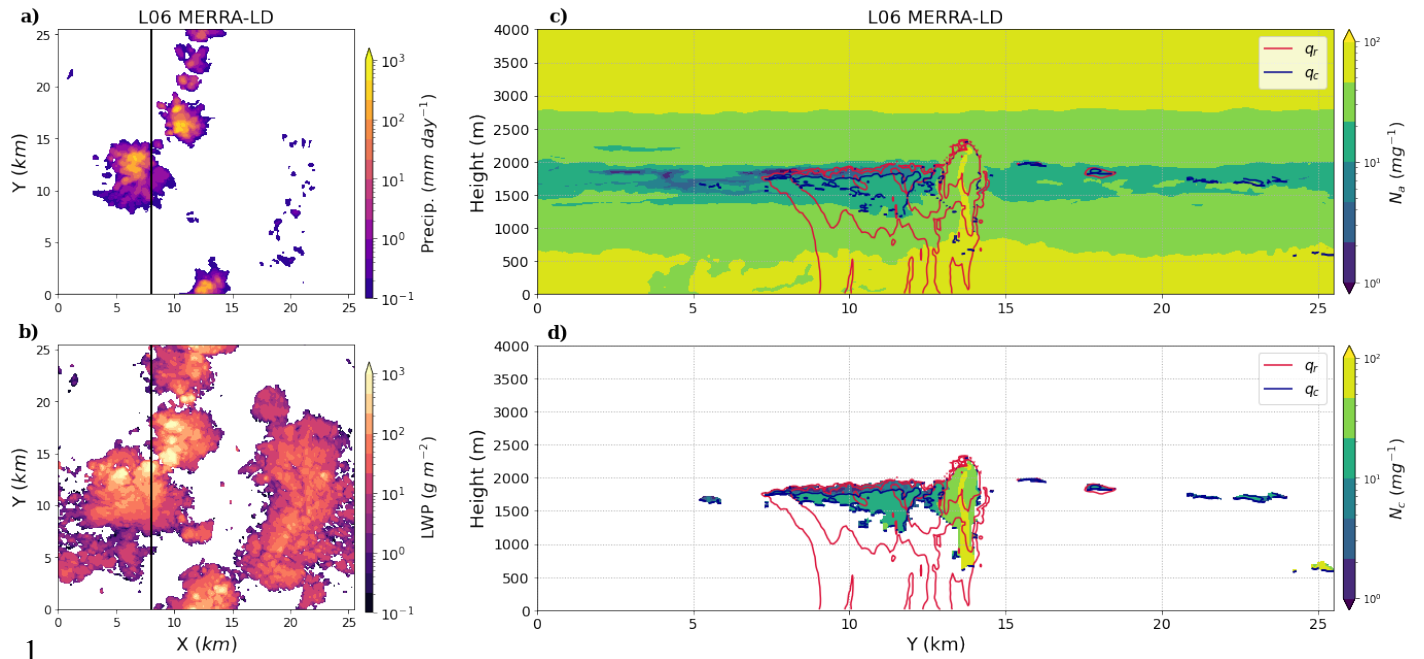
9

Figure 9. Microphysical and macrophysical variables as a function of $\langle N_c \rangle$ for the L06 (circles) and L10 (squares) cases, from both the simulations and selected observations. Variables on the y-axis are a) the short-wave cloud radiative effect (SW CRE), b) cloud LWP, c) LCC, d) surface precipitation, e) τ_c , f) r_e , g) Z_{inv} , and h) w_e . Each colored point shows results for one LES run averaged over the whole day-time period of the run. Observed values are plotted as black or gray circles for L06 and black or gray squares for L10 case. Here, the observed values of $\langle N_c \rangle$ are from GOES and the observed or reanalysis values of parameters are from sources as given in the upper-right corner of each panel.



1
 2 Figure 10. Time-height evolution of a&b) w'^2 , c&d) cloud fraction (CF) and precipitation flux, and e&f) N_a . The x-
 3 axis is time in fraction of a day relative to the time of the SCT. G&h) The vertical profiles of N_a are shown at several
 4 times near the time of the SCT. For each time, the shaded area between the two lines shows the 5th and 95th percentile
 5 range in the variable's probability distribution function (PDF). The results are for two LES runs: L06 MERRA-LD
 6 (left panels) and L10 250-60-LD (right panels).

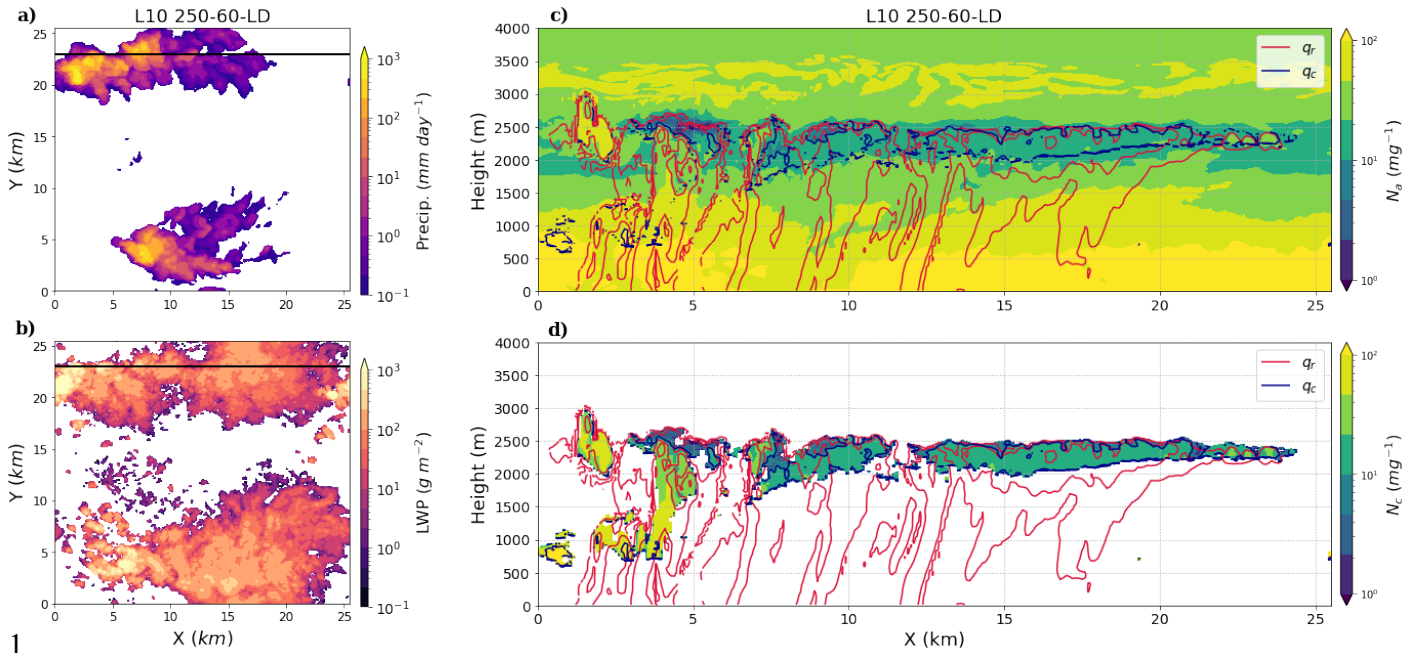
7



1
 2 Figure 11. Left panels: snapshots of a) surface precipitation, and b) cloud LWP for the L06 MERRA-LD run at a time
 3 close to the SCT, day 1.875 (relative to the run start). Right panels: y-z cross-sections of c) N_a and d) N_c , with contours
 4 of rain mass or q_r ($1e-4$, $1e-3$ kg kg^{-1}) and cloud liquid mass or q_c ($1e-5$, $1e-4$, $1e-3$ kg kg^{-1}). Cross-sections are at $x =$
 5 8 km (black lines in the left panels).

6

7

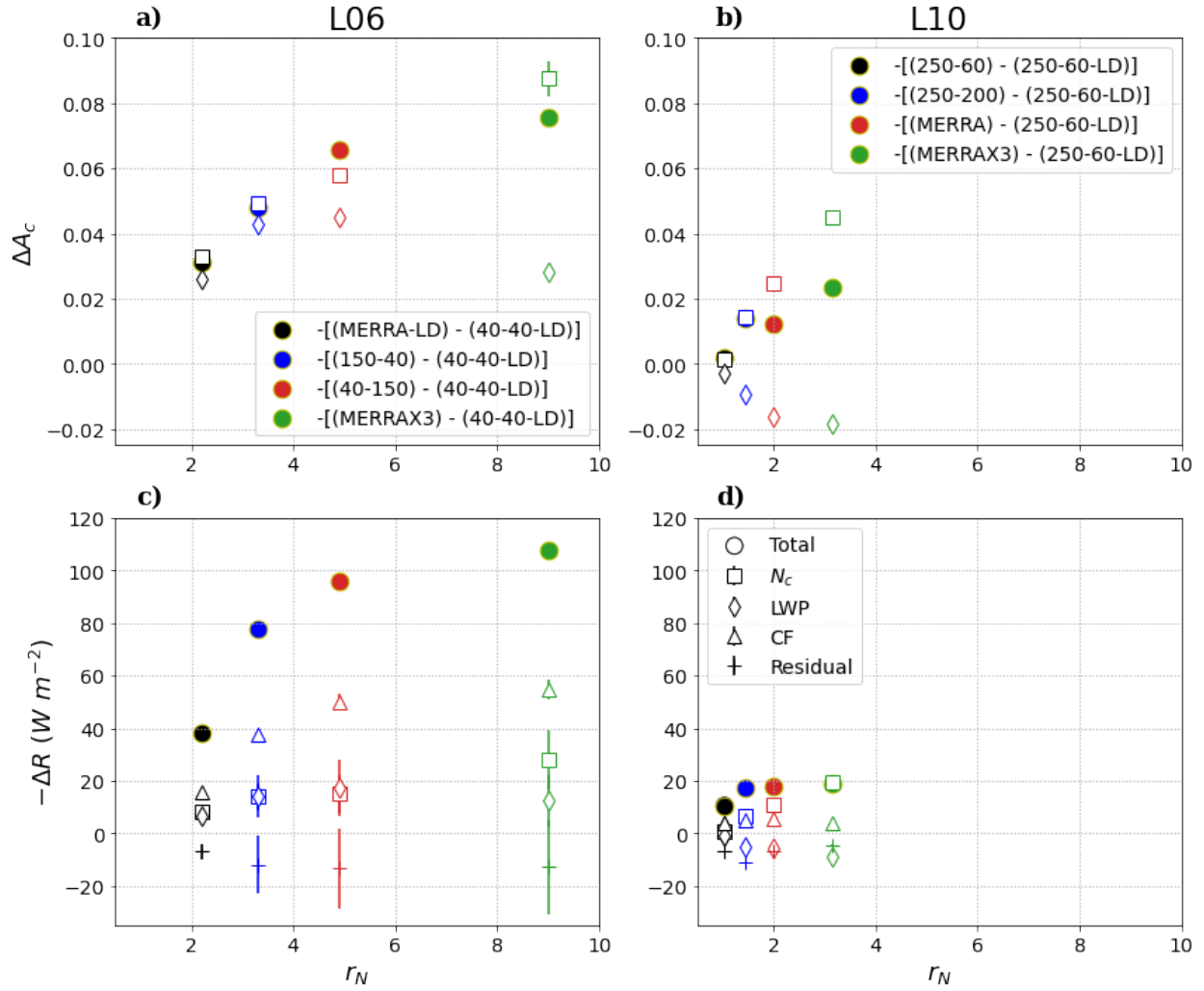


1

2 Figure 12. As in Figure 11, but for L10 250-60-LD and for x-z cross-sections at $y = 23$ km (black lines on left panels).

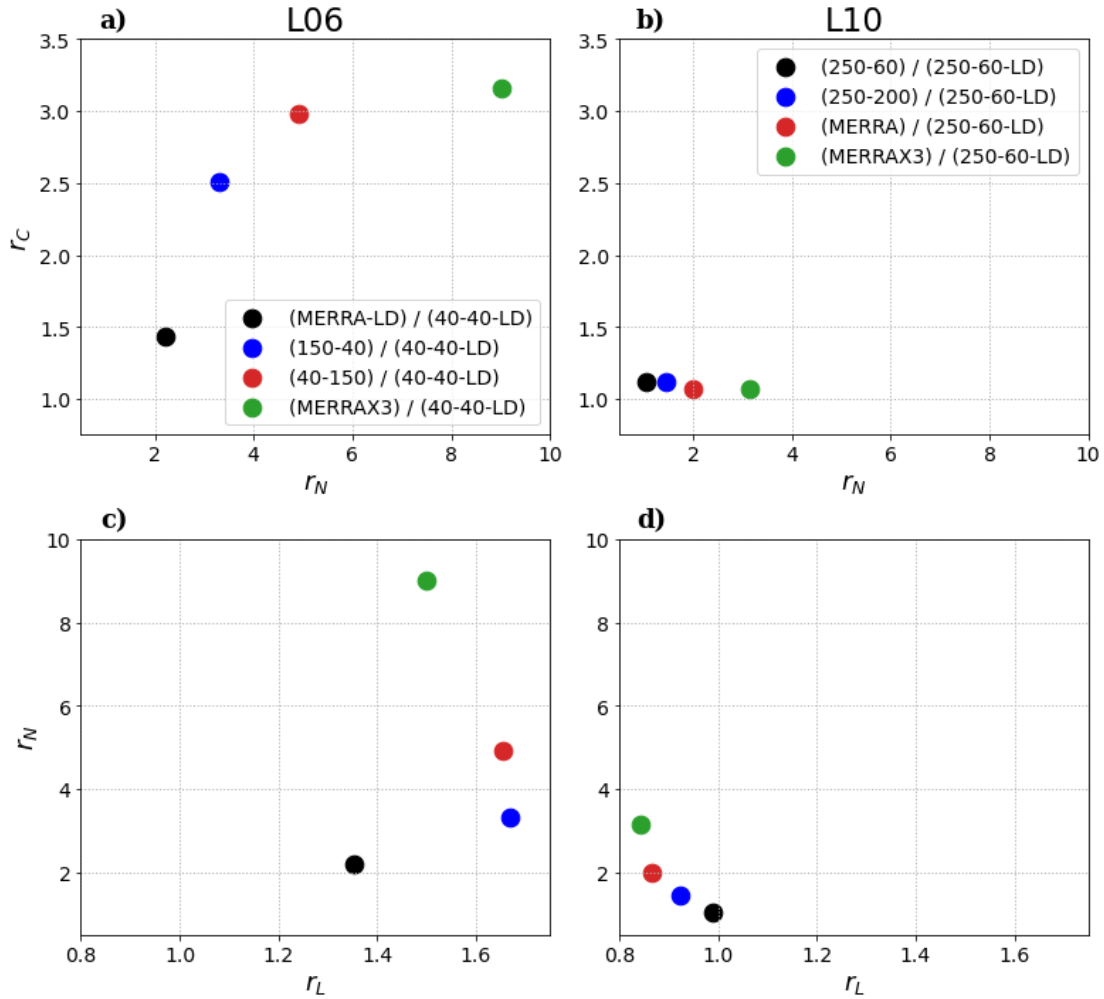
3 Here, the data are for day 3.375 relative to the run start.

4



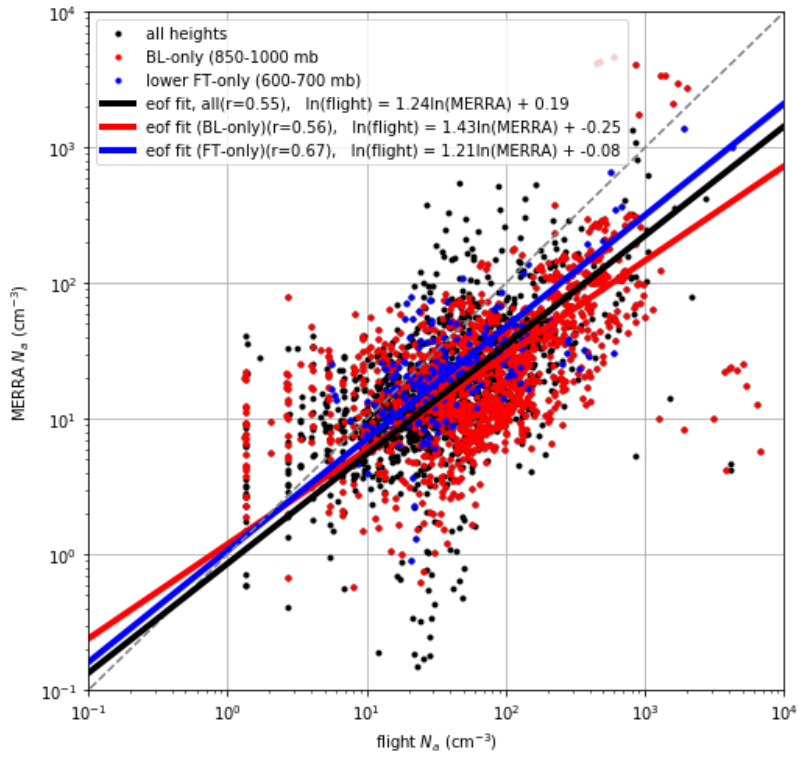
1
 2 Figure 13. Upper panels: change in cloudy-sky albedo (ΔA_c) as a function of the ratio of the perturbed to baseline
 3 cloud droplet number concentration ($r_N = \frac{N_{c2}}{N_{c1}}$) for a) L06 and b) L10. Lower panels: change in the cloud radiative
 4 effect (ΔR) as a function of r_N for c) L06 and d) L10. Each point shows the variables for a pair of LES runs with
 5 values averaged over the whole day-time period of the run. The filled circles show the total change in A_c and R
 6 between the two LES runs. The square, diamond, triangle, and plus markers, respectively, show the effects of changes
 7 in N_c , LWP, CF, and the residual (CDNC + LWP + CF - Total). The markers for N_c , LWP, CF, and residual show the
 8 results of step 3, whereas the endpoints of bars show steps 1 and 2 of the calculations described in the text.

9



1
 2 Figure 14. Upper panels: ratio of the perturbed to baseline cloud fraction ($r_C = \frac{c_2}{c_1}$) as a function of the
 3 perturbed to baseline cloud droplet number concentration ($r_N = \frac{N_{c2}}{N_{c1}}$) for the a) L06 and b) L10 cases. Lower panels:
 4 r_N as a function of the ratio of the perturbed to baseline liquid water path ($r_L = \frac{L_2}{L_1}$) for the c) L06 and d) L10 cases.
 5 Each point shows the ratio between a pair of LES runs with values averaged over the whole day-time period of the
 6 run.

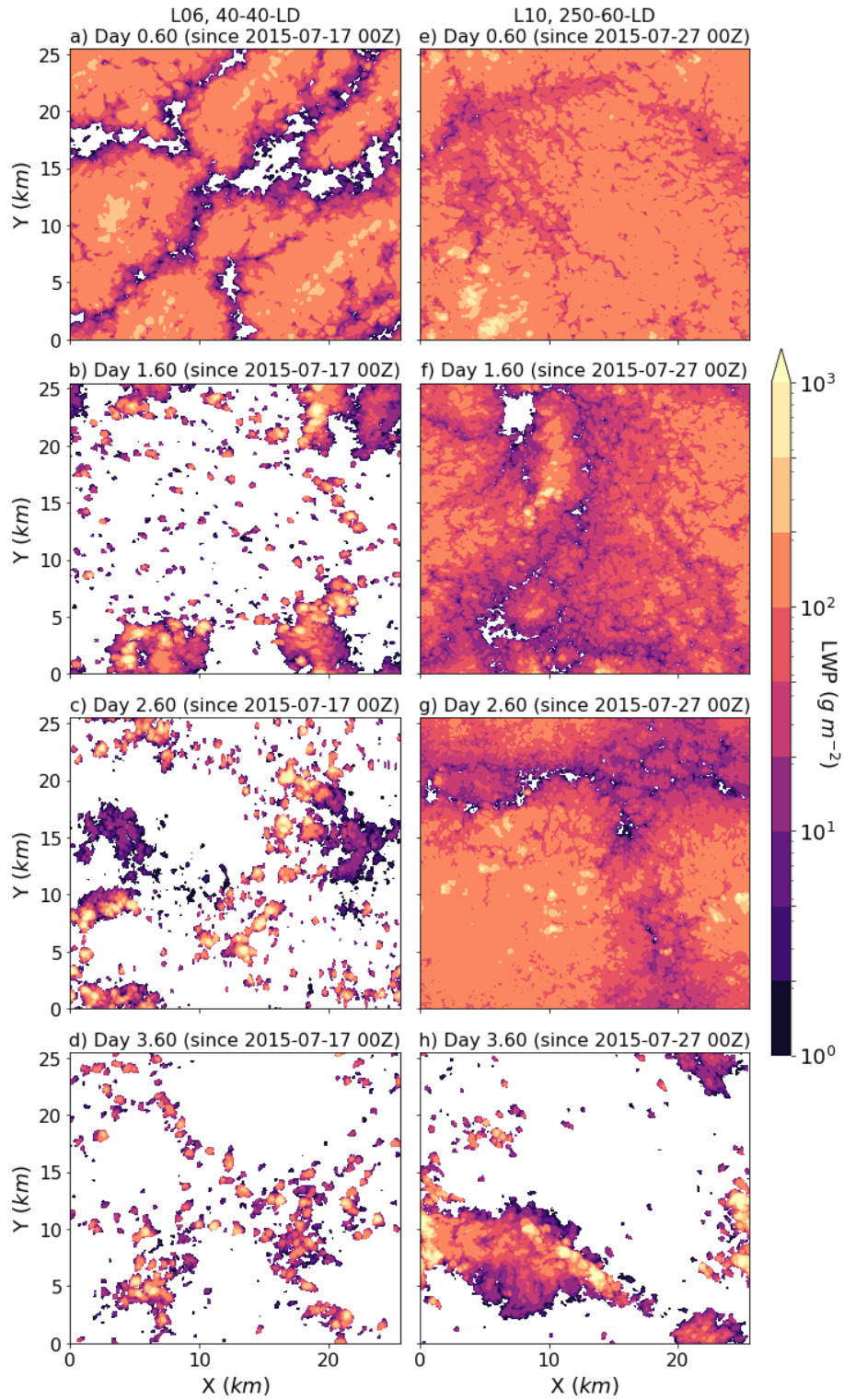
7



1

2 Figure A1. Linear regression in log-log space between N_a from all CSET flights and N_a derived from collocated
 3 MERRA2 data.

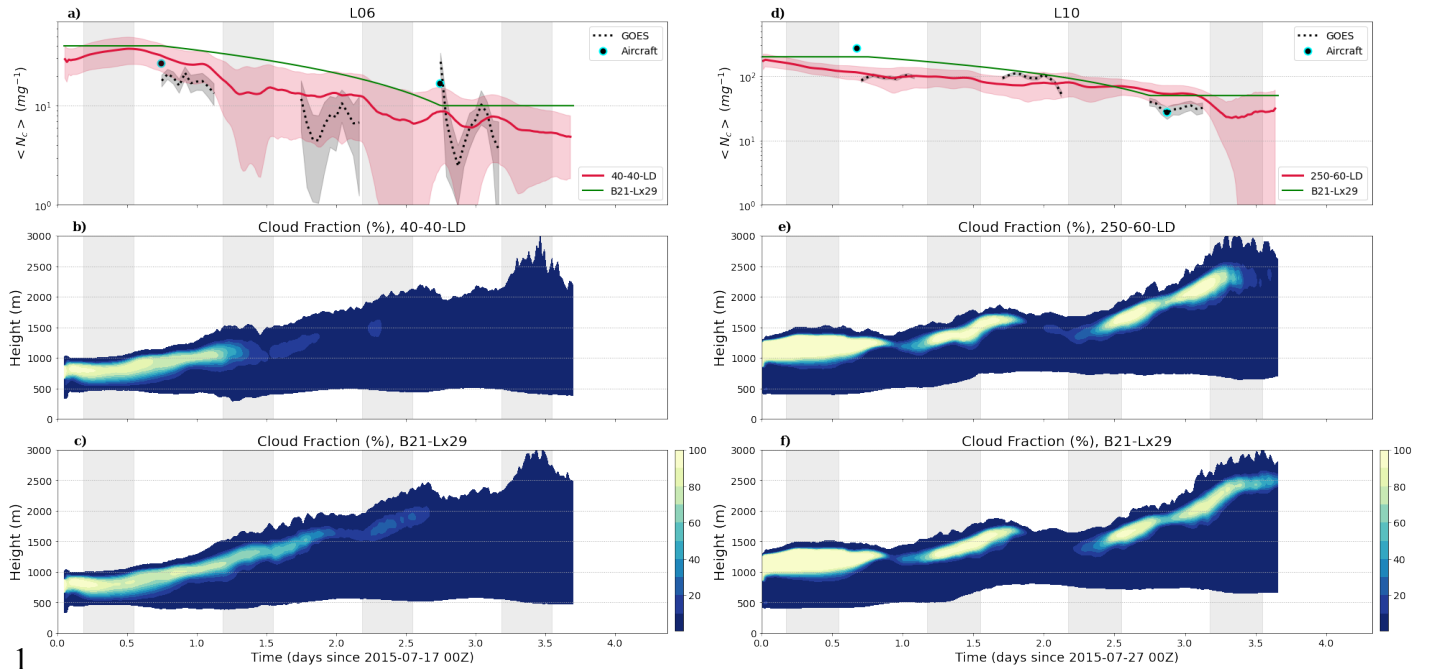
4



1

2 Figure S1. Snapshots of cloud LWP for the L06, 40-40-LD run on days a) 0.6, b) 1.6, c) 2.6 and d) 3.6 following the
 3 start of the simulation. e-h) As in a-d, but for the L10, 250-60 run.

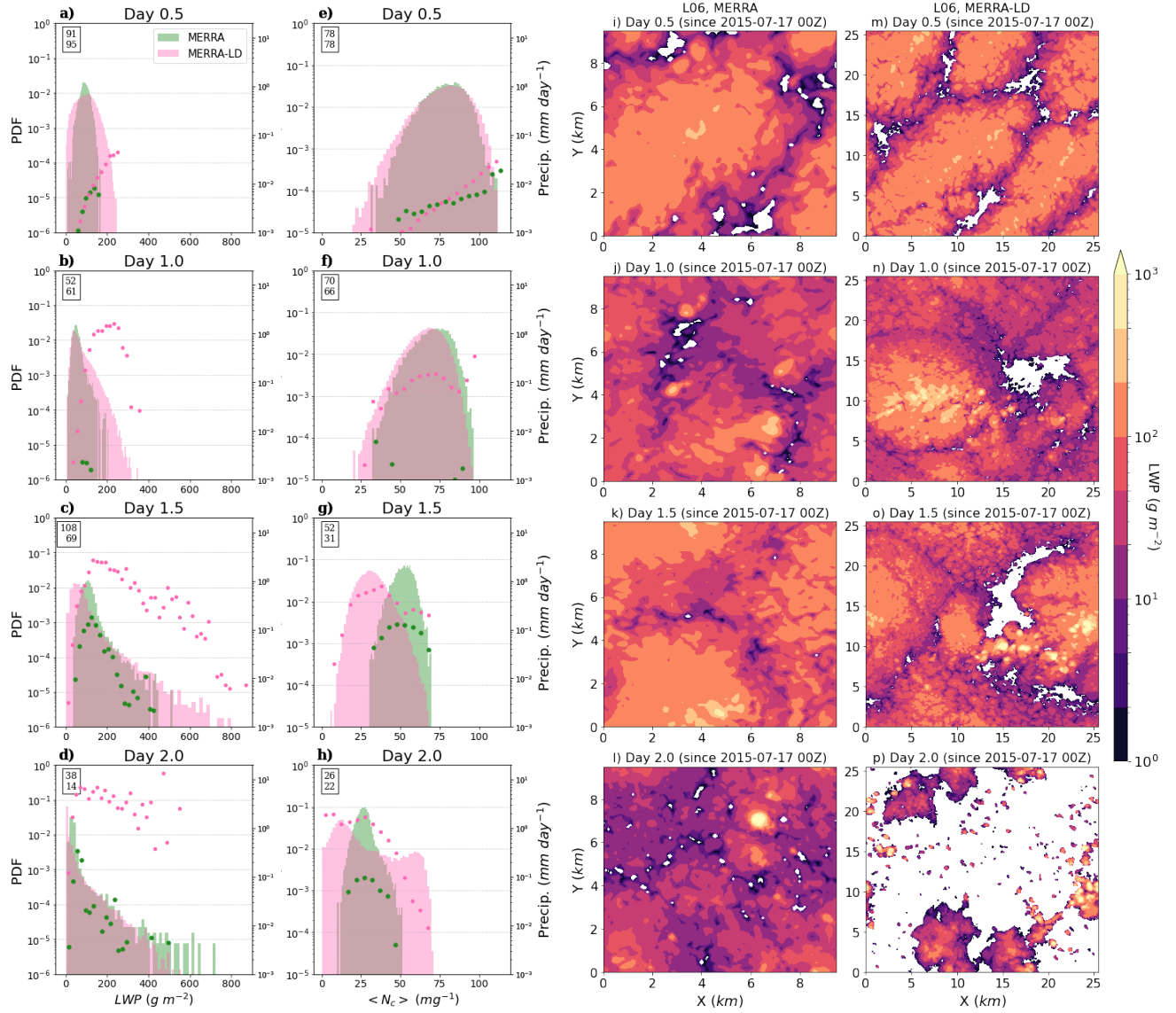
4



1

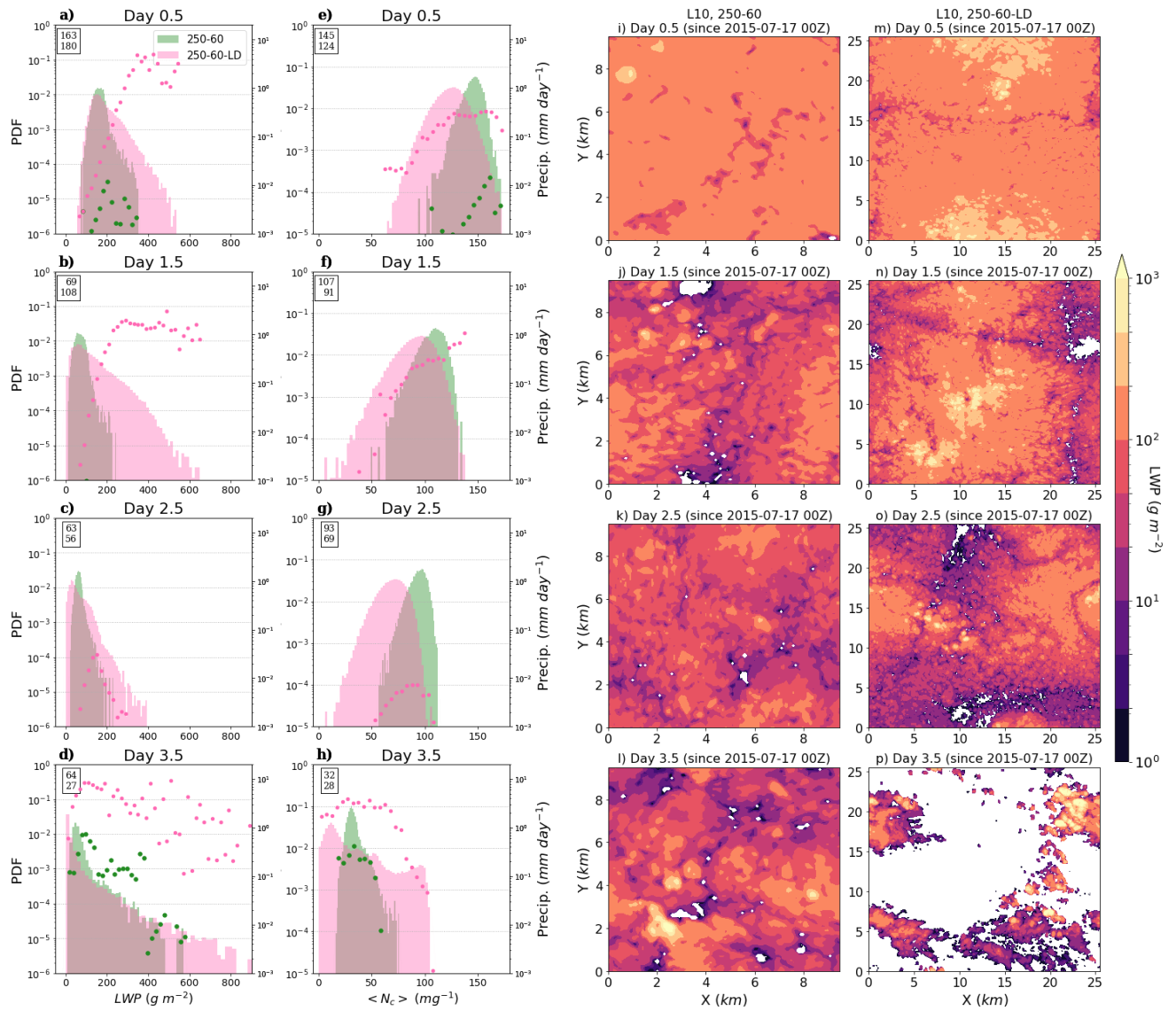
2 Figure S2. a) Time series of observed and modeled domain-averaged, MBL-averaged $\langle N_c \rangle$ for this study's L06 40-
 3 40-LD run and for the L06 Lx29 run from B21. b) Time-height evolution of domain-averaged cloud fraction for this
 4 study's L06 40-40-LD run. c) As in b, but for the L06 Lx29 run from B21. d-f) As in a-c, but for this study's L10 250-
 5 60-LD run and the L10 Lx29 run from B21.

6



1
 2 Figure S3. a-d) Probability distribution functions of cloud LWP at four times for L06, MERRA and MERRA-LD runs.
 3 The dots show precipitation in bins of LWP, and the boxes on the upper-left corner of each panel show domain-
 4 averaged LWP for MERRA (first value) and MERRA-LD (second value). Each panel shows data averaged for a period
 5 of 1 hour. e-h) as in a-d, but for $\langle N_c \rangle$. i-l) Snapshots of cloud LWP at four times for MERRA run. m-p) as in i-l, but
 6 for MERRA-LD run.

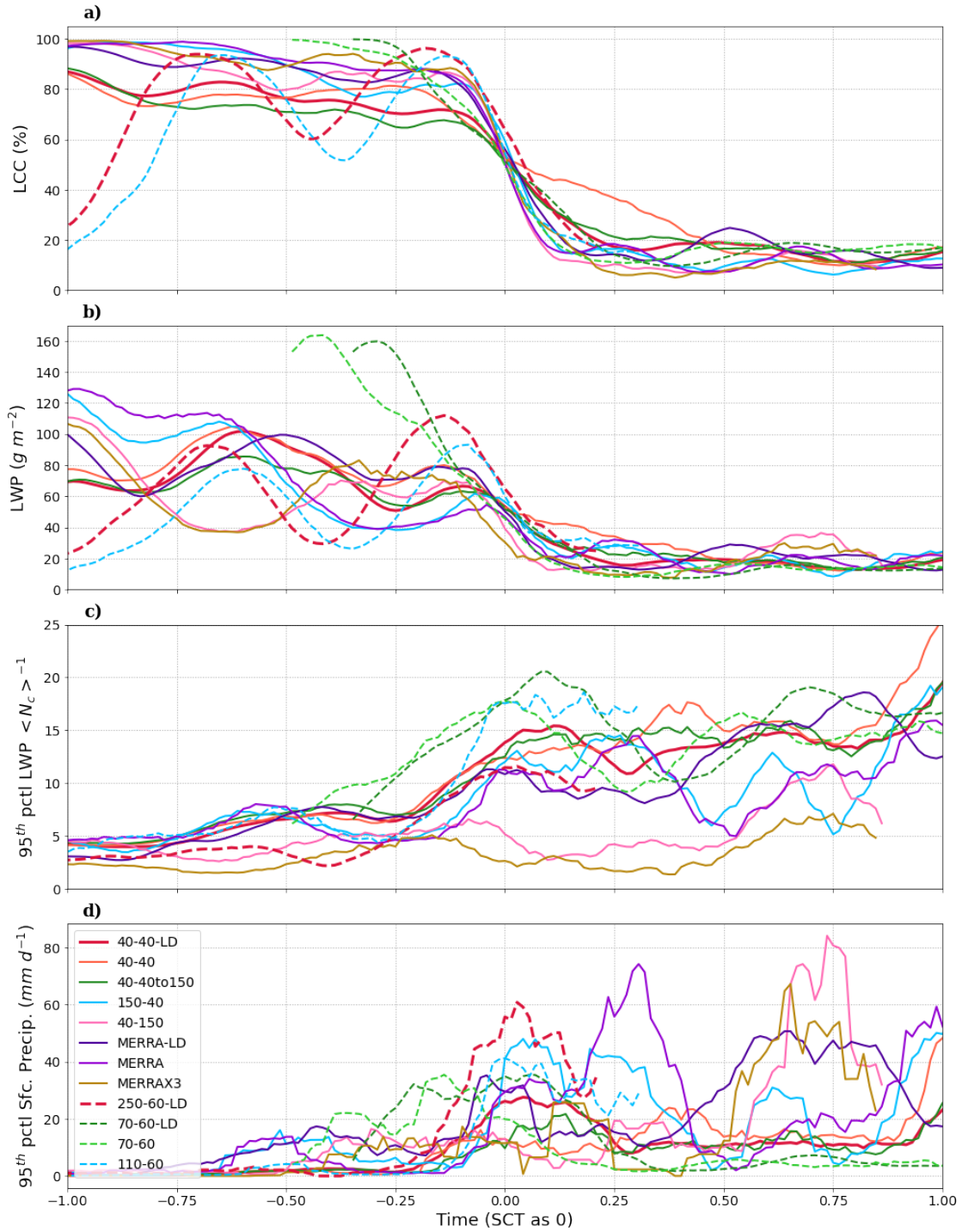
7



1

2 Fig. S4. As in Fig. S3, but for 250-60 and 250-60-LD runs.

3



1

2 Fig. S5. Time series of a) LCC, b) cloud LWP, c) 95th percentile cloud LWP $< N_c >^{-1}$, and d) 95th percentile surface
 3 precipitation for all the runs with clear SCT. The x-axis is time (in units of day) with SCT selected as 0.

4